# The JCMT Gould Belt Survey: a first look at SCUBA-2 observations of the Lupus I molecular cloud

Mowat, C.; Hatchell, J.; Rumble, D.; Kirk, H.; Buckle, J.; Berry, D. S.; Broekhoven-Fiene, H.; Currie, M. J.; Jenness, T.; Johnstone, D.; Mottram, J. C.; Pattle, K.; Tisi, S.; Di Francesco, J.; Hogerheijde, M. R.; Ward-Thompson, D.; Bastien, P.; Bresnahan, D.; Butner, H.; Chen, M.; Chrysostomou, A.; Coudé, S.; Davis, C. J.; Drabek-Maunder, E.; Duarte-Cabral, A.; Fich, M.; Fiege, J.; Friberg, P.; Friesen, R.; Fuller, G. A.; Graves, S.; Greaves, J.; Holland, W.; Joncas, G.; Kirk, J. M.; Knee, L. B. G.; Mairs, S.; Marsh, K.; Matthews, B. C.; Moriarty-Schieven, G.; Rawlings, J.; Retter,



**Publisher's version / Version de l'éditeur:**
https://doi.org/10.1093/mnras/stx042
*Monthly Notices of the Royal Astronomical Society, 467, 1, pp. 812-835, 2017-05-11*

Monthly Notices of the ROYAL ASTRONOMICAL SOCIETY

MNRAS **467,** 812–835 (2017) doi:10.1093/mnras/stx042
Advance Access publication 2017 January 11

# The JCMT Gould Belt Survey: a first look at SCUBA-2 observations of the Lupus I molecular cloud

C. Mowat,[1⋆] J. Hatchell,[1⋆] D. Rumble,[1] H. Kirk,[2] J. Buckle,[3,4] D. S. Berry,[5] H. Broekhoven-Fiene,[6] M. J. Currie,[5] T. Jenness,[5,7] D. Johnstone,[5,2,6] J. C. Mottram,[8,9] K. Pattle,[10] S. Tisi,[11] J. Di Francesco,[2,6] M. R. Hogerheijde,[8] D. Ward-Thompson,[10] P. Bastien,[12] D. Bresnahan,[10] H. Butner,[13] M. Chen,[6] A. Chrysostomou,[14] S. Coudé,[12] C. J. Davis,[15] E. Drabek-Maunder,[16] A. Duarte-Cabral,[17] M. Fich,[11] J. Fiege,[18] P. Friberg,[5] R. Friesen,[19] G. A. Fuller,[20] S. Graves,[5] J. Greaves,[17] W. Holland,[21,22] G. Joncas,[23] J. M. Kirk,[10] L. B. G. Knee,[2] S. Mairs,[6] K. Marsh,[17] B. C. Matthews,[2,6] G. Moriarty-Schieven,[2] J. Rawlings,[24] B. Retter,[1] J. Richer,[3,4] D. Robertson,[25] E. Rosolowsky,[26] S. Sadavoy,[27] H. Thomas,[5] N. Tothill,[28] S. Viti,[24] G. J. White,[29,30] J. Wouterloot,[5] J. Yates[24] and M. Zhu[31]

*Affiliations are listed at the end of the paper*

Accepted 2017 January 6. Received 2017 January 5; in original form 2016 September 22

## ABSTRACT

This paper presents observations of the Lupus I molecular cloud at 450 and 850 μm with Submillimetre Common User Bolometer Array (SCUBA-2) as part of the James Clerk Maxwell Telescope Gould Belt Survey (JCMT GBS). Nine compact sources, assumed to be the discs of young stellar objects (YSOs), 12 extended protostellar, pre-stellar and starless cores, and one isolated, low-luminosity protostar, are detected in the region. Spectral energy distributions, including submillimetre fluxes, are produced for 15 YSOs, and each is fitted with the models of Robitaille et al. The proportion of Class 0/I protostars is higher than that seen in other Gould Belt regions such as Ophiuchus and Serpens. Circumstellar disc masses are calculated for more evolved sources, while protostellar envelope masses are calculated for protostars. Up to four very low luminosity objects are found; a large fraction when compared to other *Spitzer* c2d regions. One YSO has a disc mass greater than the minimum mass solar nebula. 12 starless/protostellar cores are detected by SCUBA-2 and their masses are calculated. The stability of these cores is examined using both the thermal Jeans mass and a turbulent virial mass when possible. Two cores in Lupus I are super-Jeans and contain no known YSOs. One of these cores has a virial parameter of $1.1 \pm 0.4$, and could therefore be pre-stellar. The high ratio of Class 0/I to Class III YSOs (1:1), and the presence of a pre-stellar core candidate, provides support for the hypothesis that a shock recently triggered star formation in Lupus I.

**Key words:** catalogues – stars: formation – stars: pre-main-sequence – stars: protostars – ISM: structure – submillimetre: general.

## 1 INTRODUCTION

B228 was first catalogued by Barnard (1927), as a vacant (dark) region in the sky extending from the north-west (NW) to the south-east (SE). More recently the ridge, as well as additional nearby structure, has been collectively referred to as Lupus I (Comerón 2008). This molecular cloud is one of the closest regions of star formation to Earth. The most recent estimate of the distance to Lupus I has yielded a value of $182^{+7}_{-6}$ pc (Galli et al. 2013), although other work has produced lower estimates (e.g. the value of $155 \pm 8$ pc; Lombardi, Lada & Alves 2008). As the value from Galli et al. (2013) is recent, well constrained and calculated specifically for Lupus I (as opposed to the whole Lupus complex), this is adopted here as the

⋆ E-mail: cmowat@astro.ex.ac.uk (CM); hatchell@astro.ex.ac.uk (JH)

distance to Lupus I. Extinction maps of the region (Cambrésy 1999) as well as molecular line surveys (e.g. CO; Tachihara et al. 2001) point to a total mass of molecular gas in Lupus I of the order of $10^4$ $M_\odot$.

Lupus I sits on the edge of the Scorpius–Centaurus OB association, a nearby group of high-mass stars (see e.g. Preibisch et al. 2002). The median age of stars in the closest subgroup of Sco-Cen, Upper Centaurus-Lupus, is estimated at 16 Myr (Pecaut, Mamajek & Bubar 2012). Thus, the association is older than the YSOs in Lupus I itself, for which Hughes et al. (1994) found an age range between 0.76 and 3.16 Myr. There is also ongoing star formation in the region, an example being the Class 0 protostar IRAS 15398-3359 (Oya et al. 2014). Stars in Lupus I are also noted by Hughes et al. (1994) to be younger than those of Lupus III; Tachihara et al. (1996) suggest this could be the result of a shock from Sco-Cen across Lupus I, which is closer to Sco-Cen than Lupus III.

The Lupus molecular clouds are associated with the ring of nearby OB stars and molecular clouds known as the Gould Belt. The James Clerk Maxwell Telescope (JCMT) Gould Belt Legacy Survey (GBS; Ward-Thompson et al. 2007) was initiated to map all nearby star-forming regions accessible from Maunakea with the Submillimetre Common User Bolometer Array (SCUBA-2; Holland et al. 2013). SCUBA-2 is capable of producing maps of submillimetre continuum emission over extended areas of the sky.

Detections in the submillimetre enable the amount of cold material to be estimated. Hence, masses of circumstellar disc for more evolved sources (e.g. Buckle et al. 2015; Dodds et al. 2015) or circumstellar envelopes for more embedded sources (e.g. Rumble et al. 2015) can be determined. 870 μm observations of Lupus I by Gaczkowski et al. (2015) have already enabled the detection of dense cores and the estimation of their masses. This work uses the SCUBA-2 continuum maps of Lupus I to study the population of young stellar objects (YSOs), largely identified from *Spitzer Space Telescope* observations (Merín et al. 2008), as well as dense cores and their stability.

The structure of this paper is as follows. Section 2 discusses the observations and data reduction process. Section 3 presents the final SCUBA-2 maps of Lupus I. Section 4 focuses on the YSOs found in Lupus I. Disc properties are explored, and spectral energy distributions (SEDs) of the known YSOs in the region are produced by combining SCUBA-2 data with data from a variety of other surveys. Extended structures, treated as protostellar, pre-stellar and starless cores, are examined in Section 5. The size and stability of these cores is evaluated. In Section 6, the conclusions of this paper are summarized.

## 2 OBSERVATIONS AND DATA REDUCTION

Three separate fields in the Lupus I molecular cloud were observed with SCUBA-2 (Holland et al. 2013) as part of the JCMT GBS (Ward-Thompson et al. 2007). Continuum observations at both 850 and 450 μm were made using the PONG mapping pattern (Kackley et al. 2010) to produce 30 arcmin diameter maps of each field (designated NW, E and SW). Observations can probe extended structure down to the scale of the JCMT effective beam size, approximately 9.6 arcsec at 450 μm and 14.1 arcsec at 850 μm (Dempsey et al. 2013). The JCMT beam can be described as a superposition of both a main-beam Gaussian and an error-beam Gaussian. The secondary error beam is larger than the effective size of the main beam, 48 and 25 arcsec at 850 and 450 μm, respectively.

Three scans of the NW field were taken in 2014 August, with the rest of the scans of Lupus I taken in 2015 January. The sky coordinates (J2000) on which the NW, E and SW fields are centred, along with other details of the observations, are given in Table 1.

Most of these observations were completed in dry band 2 weather, with 225 GHz opacity $0.05 < \tau_{225} < 0.08$. $\tau_{225}$ is related to precipitable water vapour (PWV) via the relation $\tau_{225} = 0.04\mathrm{PWV}_{\mathrm{zenith}} + 0.017$ (Dempsey et al. 2013). Observation 72 of the E field on January 17, as well as observation 40 of the SW field on January 26, were made in band 3 weather, where $0.08 < \tau_{225} < 0.12$. Finally, observation 46 of the SW field on January 26 was in poorer band 4 weather, with $\tau_{225} = 0.13$. While observations at 850 μm can be successfully carried out in as low as band 3 weather, 450 μm observations begin to degrade even in dry band 2 conditions.

Data reduction was implemented with MAKEMAP, an iterative map-maker that is part of the Submillimetre User Reduction Facility (SMURF; Chapin et al. 2013). The data reduction for this analysis is consistent with the GBS Legacy Release 1, including gridding data to 3 arcsec pixels at 850 μm and 2 arcsec pixels at 450 μm. However, there are a few differences that will be highlighted.

A two-stage data reduction process is used to produce the final SCUBA-2 maps in this paper and the GBS Legacy Release 1 data set in general. The first map produced, the automask reduction, uses high signal-to-noise ratio (SNR) values in the SCUBA-2 timestream to identify real sources of emission. The second 'external mask' reduction uses a combination of stacked automask reductions and other available information to constrain areas of real source emission for the reduction. In both rounds of reduction, models of the various modes of emission (including common mode subtraction, high pass filtering and real astronomical signal; Chapin et al. 2013) are iterated upon until the average change of the pixels in the map between iterations is reduced to <0.1 per cent of the map rms.

**Table 1.** Full catalogue of JCMT MJLSG34 observations of Lupus I. $\tau_{225}$ is the opacity of the atmosphere at 225 GHz when each observation was undertaken.

| | North-west $15^h42^m45^s$ $-34°04'31''$ | | | East $15^h45^m22^s$ $-34°21'33''$ | | | South-west $15^h39^m33^s$ $-34°41'31''$ | | |
|---|---|---|---|---|---|---|---|---|---|
| Scan # | Date | Obs # | $\tau_{225}$ | Date | Obs # | $\tau_{225}$ | Date | Obs # | $\tau_{225}$ |
| 1 | 2014/08/15 | 00011 | 0.08 | 2015/01/17 | 00068 | 0.07 | 2015/01/22 | 00079 | 0.07 |
| 2 | 2014/08/21 | 00024 | 0.06 | 2015/01/17 | 00072 | 0.09 | 2015/01/22 | 00087 | 0.06 |
| 3 | 2014/08/22 | 00013 | 0.05 | 2015/01/17 | 00078 | 0.07 | 2015/01/24 | 00061 | 0.08 |
| 4 | 2015/01/13 | 00067 | 0.06 | 2015/01/20 | 00062 | 0.06 | 2015/01/24 | 00066 | 0.07 |
| 5 | 2015/01/13 | 00068 | 0.05 | 2015/01/20 | 00066 | 0.06 | 2015/01/26 | 00040 | 0.10 |
| 6 | 2015/01/15 | 00080 | 0.06 | 2015/01/20 | 00071 | 0.05 | 2015/01/26 | 00042 | 0.07 |
| 7 | ... | ... | ... | ... | ... | ... | 2015/01/26 | 00046 | 0.13 |

Parameters for the automask reductions for Lupus I differ from Legacy Release 1 in order to improve the recovery of faint emission. Based on the tests by Mairs et al. (2015), lower SNR pixels were considered as potential source emission by changing the value of the ast.zero_snr parameter from 5 to 3. Additionally, zones of probable source emission were extended from none below a $5\sigma$ floor to include $2\sigma$ pixels around a $3\sigma$ peak, by changing the ast.zero_snrlo parameter from 0 to 2. A similar procedure will be used in the next GBS data release.

Individual automask-reduced maps for each field were then co-added into mosaics using the PICARD recipe MOSAIC_JCMT_IMAGES (Gibb, Jenness & Economou 2013). The presence of noisy data artefacts in the August 15 scan of the NW field resulted in this scan being excluded from this process, which increased the overall noise of the NW field automask mosaic. The 850 μm mosaics were used to identify probable emission structure in order to create masks for use in the extmask reduction stage. Every individual pixel in the SCUBA-2 maps with an SNR of at least one was included in the masks produced. While this criterion inevitably included fake as well as real emission, masked 'fake' pixels are non-contiguous. Hence, they are not reproduced in the external mask reduction stage.

At 850 μm, the SCUBA-2 masking for the SW field was combined with the *Herschel* 500 μm (Rygl et al. 2013) continuum map, masking off emission below a 1 Jy beam$^{-1}$ threshold. Additionally, circular masks of 1 arcsec diameter centred around *Spitzer*-identified sources from Merín et al. (2008) were used. All pixels within these masks could therefore be considered as potential emission structure. The extra masking was used due to faint emission in the field. Pixels below the SNR of 3 required to be treated as a zone of emission in the automask reduction stage could none the less visibly correspond to areas of real emission seen in the *Herschel* map.

The 450 μm masks were generally the same as at 850 μm. However, for the SW field, only SCUBA-2 850 μm contours were used, simply because the quality of the observations was so low that no form of masking would be able to extract true signal from the noise. This situation is detailed in Section 3.

The masks (Fig. 1, available in the online-only supporting information) were then used in the external mask reduction stage. The iterative map-maker was re-run using these masks, and all fields were then mosaicked together to produce final maps of the Lupus I molecular cloud at both 850 and 450 μm. All scans were used to produce the final maps, in order to obtain the best SNR for areas of real emission. However, this approach does allow the possibility of data artefacts in individual scans propagating through to the final map. Such artefacts are present in one scan of the NW field (see Fig. 1).

The data reductions used a spatial filter of 10 arcsec, meaning that sources with a Gaussian full width at half-maximum (FWHM) size of $<$2.5 arcmin are robustly detected. Sources with 2.5 arcmin $<$ FWHM $<$ 7.5 arcmin will be detected, but with both flux and size underestimated. Any sources larger than this will depend on the mask being used in the data reduction, or they will be suppressed (Chapin et al. 2013). The tests of Mairs et al. (2015) show that extended structure is suppressed during the data reduction when located outside an external mask. Small-scale structures do not suffer from being located outside the mask to nearly the same extent.

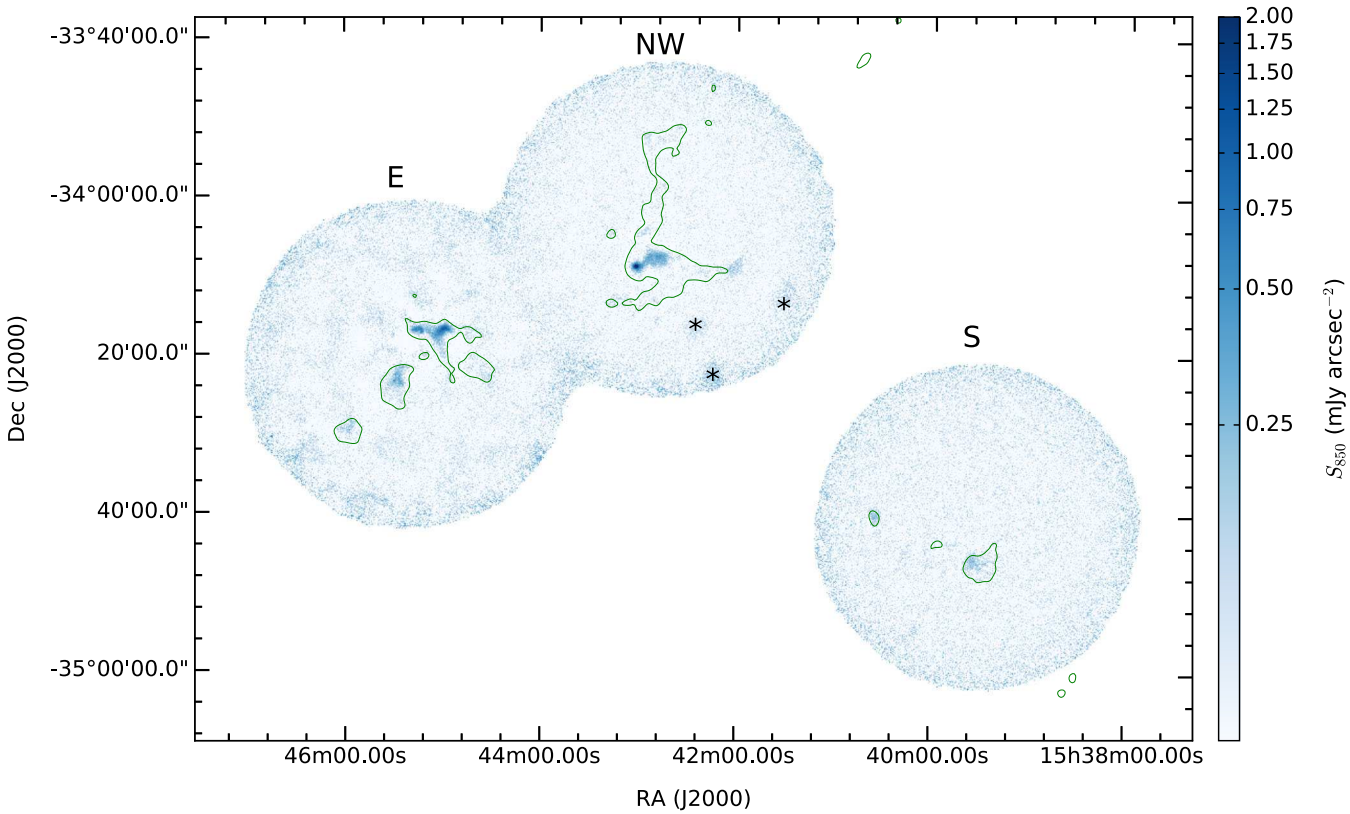


**Figure 1.** SCUBA-2 850 μm dust continuum map of the Lupus I molecular cloud. Noisy edges of the three fields have been largely removed from the map. Artefacts in the data from the August 15 scan of the NW field, in the bottom right of the field, are marked with asterisks. *Herschel* 500 μm emission (Rygl et al. 2013) is shown with green contours, at a level of 30 MJy sr$^{-1}$.

The data are calibrated to units of mJy arcsec$^{-2}$ using flux conversion factors in the data reductions of 21.06 ± 0.72 and 18.84 ± 2.00 Jy pW$^{-1}$ pixel$^{-1}$ at 850 and 450 μm, respectively. Due to the chosen pixel sizes of 3 and 2 arcsec at 850 and 450 μm, respectively, these numbers therefore correspond to the values of 2.34 ± 0.08 and 4.71 ± 0.5 Jy pW$^{-1}$ arcsec$^{-2}$ in Dempsey et al. (2013).

All of the data products presented in this paper are available at: http://dx.doi.org/10.11570/17.0002.

## 3 SCUBA-2 MAPS

The reduced SCUBA-2 maps of Lupus I are shown in Fig. 1 (850 μm) and Fig. 2 (450 μm). The typical pixel-to-pixel rms noise level at 850 μm is 0.06 mJy arcsec$^{-2}$. Noise is larger and more variable at 450 μm, with values of 1.7, 2.8 and 5.1 mJy arcsec$^{-2}$ for the NW, E and SW fields, respectively. The noisy edges of these fields were clipped using the Starlink KAPPA software (Currie & Berry 2013) to remove edge areas with incomplete PONG coverage (with a local noise level of greater than 0.1 mJy arcsec$^{-2}$). Due to the widely varying noise levels in the 450 μm map, this strategy resulted in more clipping of the noisier fields, SW in particular. Full SCUBA-2 error maps of the region are presented in the online-only supporting information, as Fig. 3.

The 850 μm map shows evidence for both compact sources and more extended structures. The chief area of emission is seen in a line from the SE to NW corners of the E field, corresponding with the areas of extended filamentary structure seen in the *Herschel* maps of the region (Rygl et al. 2013). Additionally, the strong emission seen in the NW field is associated with the protostar IRAS 15398-3359 (Heyer & Graham 1989; Oya et al. 2014). Both the emission from the envelope of the star itself and an associated filamentary-like structure can be seen. Areas of faint, extended emission can also be seen in the SW field. The NW field is affected by the data artefacts in the 2014/08/15 scan (denoted with asterisks in Fig. 1).

In the 450 μm map, the protostar in the NW field (IRAS 15398-3359) as well as nearby extended structure can be seen. Also visible is the cluster of emission found in the centre of the E field, though there are many noisy pixels.

Some of the compact sources (assumed to be point sources) found in the 850 μm map are isolated, for example, at the SE corner of the E field. The positions of many, however, are found within the areas of extended emission. Compact sources can be seen within the cluster of emission in the E field and also in the centre of the SW field. These compact sources are expected to correspond to circumstellar discs around young stars, because SCUBA-2 does not have the required resolution to resolve discs. Taking the distance to Lupus I to be $182^{+7}_{-6}$ pc (Galli et al. 2013), the 850 μm beam size (14.1 arcsec) corresponds to a spatial scale of ∼2500 au, and the 450 μm beam size to ∼1750 au. This large extent means that the spatial scales of circumstellar discs, usually <1000 au (McKee & Ostriker 2007) and

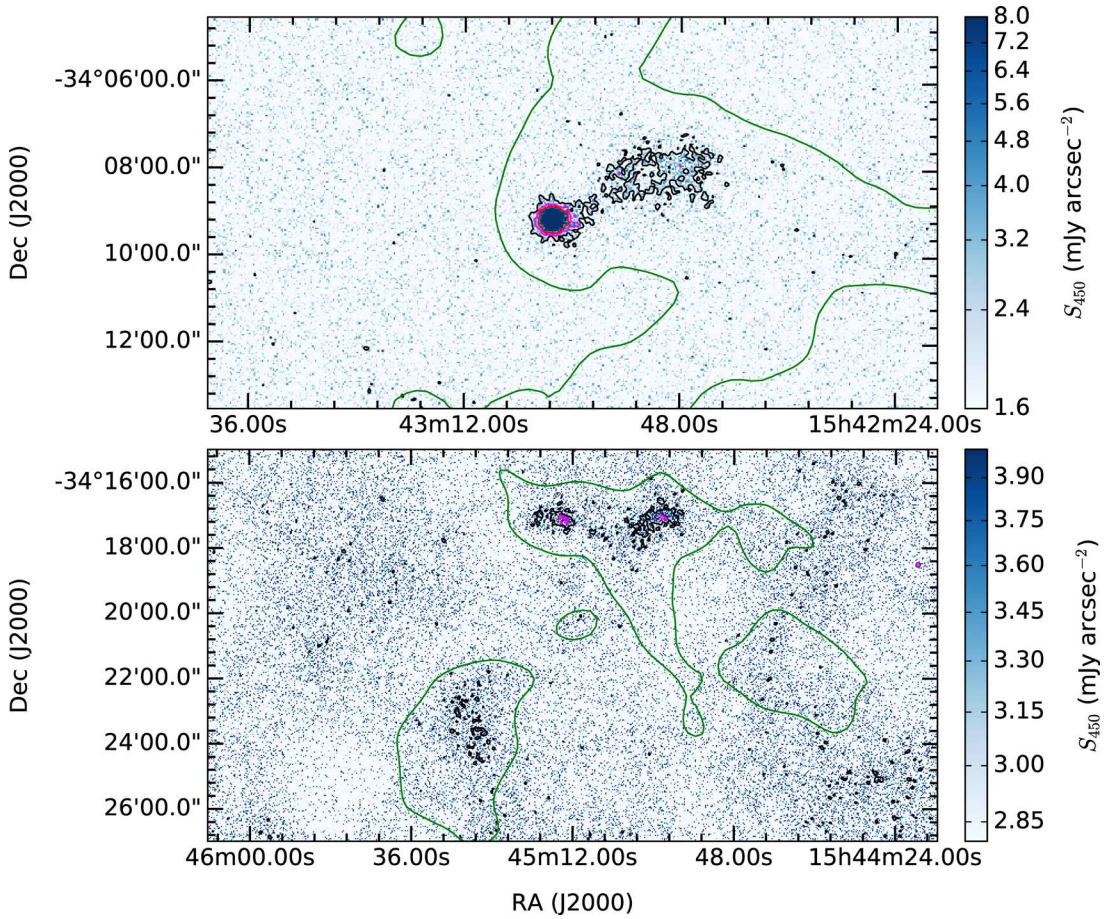


**Figure 2.** SCUBA-2 450 μm dust continuum maps of the Lupus I molecular cloud NW (top) and E (bottom) fields. Only regions containing significant detections are shown. Contours signify emission at 1$\sigma$, 2$\sigma$ and 3$\sigma$ (black, magenta and red, respectively, in the online version). *Herschel* 500 μm emission (Rygl et al. 2013) is shown with large-scale, smoothed contours (green in the online version), at a level of 30 mJy sr$^{-1}$.

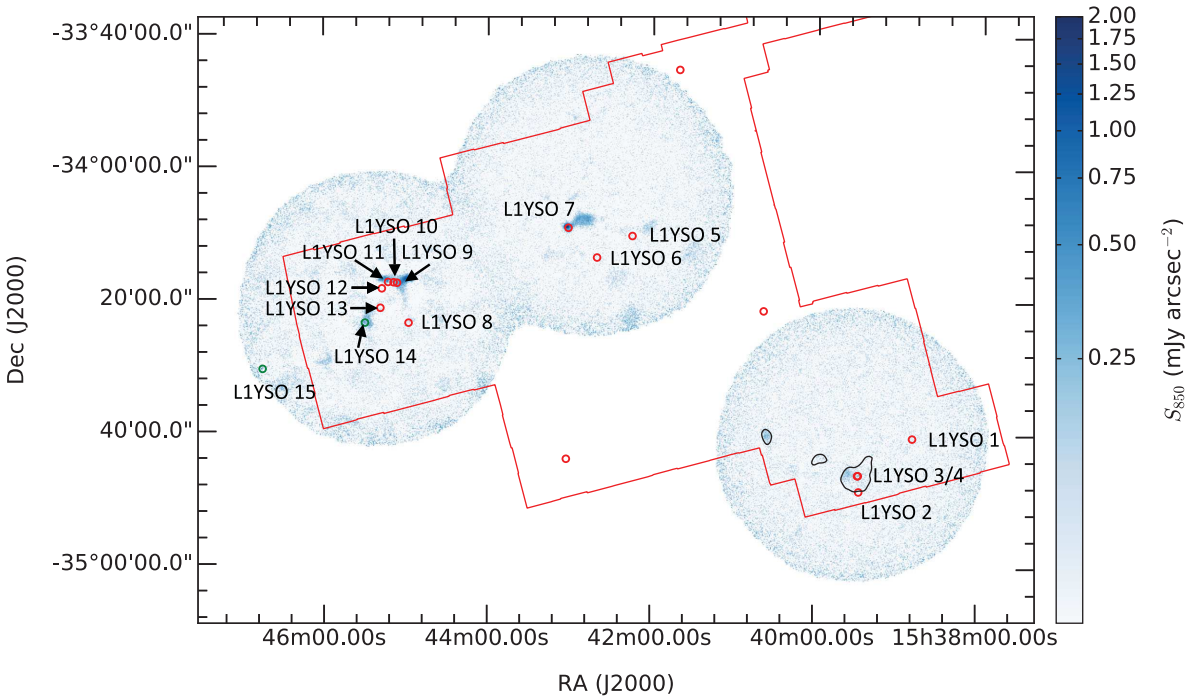


**Figure 3.** SCUBA-2 dust continuum map of the Lupus I molecular cloud at 850 μm. Additional masking contours produced from the Herschel 500 μm Lupus map (Rygl et al. 2013) are shown, and *Spitzer* YSO positions are overlaid. *Herschel* masking contours are black at the threshold used in the data reduction stage of 1 Jy. Red circles on the 850 μm map denote the position of YSOs detected by *Spitzer* (Merín et al. 2008), as detailed in Table 2. Green circles correspond to those disc sources not in the *Spitzer* paper that were detected by IRAS (labelled as L1YSO 14 and L1YSO 15). The straight red contours outline the field of view of IRAC in Lupus I.

averaging ∼200 au (Andrews & Williams 2007), fall well within the JCMT beam sizes. Hence, they are simply observed as point sources.

Overall, the amount of structure visible with SCUBA-2 in Lupus I is low. Compared to other regions observed with SCUBA-2, e.g. Ophiuchus (Pattle et al. 2015), Orion A (Salji et al. 2015; Mairs et al. 2016), Orion B (Kirk et al. 2016) and Perseus (Chen et al. 2016), the maps show much less evidence of bright, compact objects and clustered structures. Its appearance is more in line with the relatively quiescent Auriga–California Nebula (Broekhoven-Fiene et al., in preparation), although even Auriga–California contains more structure than Lupus I. Nevertheless, Lupus I contains several YSOs (see Section 4) and dense cores (see Section 5).

## 4 YOUNG STELLAR OBJECTS

### 4.1 YSO fluxes and previous observations

#### *4.1.1 SCUBA-2 Fluxes*

The Lupus I molecular cloud was observed as part of the *Spitzer* c2d project ('From Molecular Cores to Planet-Forming Discs'; Evans et al. 2003, 2009), using the *Spitzer Space Telescope* (Werner et al. 2004). Observations of Lupus I with *Spitzer* were presented in Merín et al. (2008), and the positions of 13 YSOs are used to guide photometry within the area of Lupus I observed by SCUBA-2. An additional four YSOs present in Merín et al. (2008) are outside the SCUBA-2 field of view. Source positions and the *Spitzer* area of coverage are presented, overlaid on the SCUBA-2 850 μm map, in Fig. 3. Zoomed-in 850 μm images of each of the YSOs are available in the online-only supporting information, as Fig. 2.

Photometry was also carried out for two additional sources. The source IRAS 15422-3414 (L1YSO 14) is visibly present in the Infrared Array Camera (IRAC)/Multiband Imaging Photometer for Spitzer (MIPS) observations of the region, but was excluded from Chapman et al. (2007) and Merín et al. (2008) due to being missed by the automated YSO detection criteria. Outside of the *Spitzer* coverage region, a detection was obtained of the T-Tauri star GW Lup (e.g. Kukarkin et al. 1971; Cutri et al. 2003) at 850 μm (L1YSO 15). This source was not within the 450 μm field of view due to the noisy edge clipping discussed in Section 2. Note that all YSOs examined in this work have been previously observed; no new YSOs are found.

Source fluxes were extracted using the Starlink *Gaia* image display and analysis tool (Draper et al. 2009). Apertures were centred on the literature positions of sources. At 450 μm, apertures with a diameter of 20 arcsec were used for all sources. The total flux within the apertures was extracted and annuli, with inner radii at 1.5 times the aperture radius and outer radii at 2.0 times the aperture radius, were used to estimate a background flux that was then subtracted.

At 850 μm, 20 arcsec diameter apertures were used for most sources. For the binary of IK Lup/Sz 65 (L1YSO 3) and Sz 66 (L1YSO 4), which is unresolved in the SCUBA-2 map, as well as L1YSO 10, 30 arcsec diameter apertures were used instead. These sources visibly extend beyond a 20 arcsec aperture in the 850 μm map. As they are not separately resolved, flux values for each of the sources in the binary are detected as one combined value by SCUBA-2 (as well as AKARI, InfraRed Astronomical Satellite, IRAS, and Swedish-ESO Submillimetre Telescope, SEST). To plot SEDs for the L1YSO 3/4 binary, observed fluxes were divided according to the average ratio between IRAC and MIPS fluxes, as given in Table 3. Since the SCUBA-2 detection itself was of

**Table 2.** SCUBA-2 450 and 850 μm fluxes for YSOs identified by *Spitzer* (Merín et al. 2008), with additional IRAS sources (Beichman et al. 1988). Aperture diameters used to extract flux at 850 μm are provided.

| SCUBA-2 ID | SSTc2d/IRAS ID | $S_{450}$ (mJy) | $S_{850}$ (mJy) | 850 μm Aperture (arcsec) |
|---|---|---|---|---|
| L1YSO 1 | J153848.2-344041 | ≤ 308.97 | 38.22 ± 5.61 | 20 |
| L1YSO 2 | J153927.3-344844 | ≤ 308.97 | ≤ 8.46 | 20 |
| L1YSO 3 | J153927.8-344617 | ≤ 308.97 | 80.89 ± 8.24 | 30 |
| L1YSO 4 | J153928.3-344618 | ≤ 308.97 | 80.89 ± 8.24 | 30 |
| L1YSO 5 | J154214.6-341026 | ≤ 99.18 | ≤ 7.05 | 20 |
| L1YSO 6 | J154240.3-341343 | ≤ 99.18 | ≤ 7.05 | 20 |
| L1YSO 7 | J154301.3-340915 | 18 266.00 ± 2499.38 | 3508.56 ± 150.81 | 80 |
| L1YSO 8 | J154457.9-342340 | ≤ 170.72 | 12.93 ± 3.84 | 20 |
| L1YSO 9 | J154506.3-341738 | ≤ 170.72 | 24.62 ± 6.83 | 20 |
| L1YSO 10 | J154508.9-341734 | 580.17 ± 191.32 | 56.78 ± 9.49 | 30 |
| L1YSO 11 | J154512.9-341731 | 609.78 ± 227.60 | 187.49 ± 62.03 | 20 |
| L1YSO 12 | J154517.4-341829 | ≤ 170.72 | 19.38 ± 5.29 | 20 |
| L1YSO 13 | J154518.5-342125 | ≤ 170.72 | ≤ 8.46 | 20 |
| L1YSO 14 | IRAS 15422-3414 | 327.42 ± 155.32 | 67.96 ± 7.61 | 20 |
| L1YSO 15 | IRAS 15435-3421 | ...[a] | 133.09 ± 24.96 | 20 |

*Note.* Aperture sizes at 450 μm are all 20 arcsec in diameter.
[a]No value is given here as the source is outside the error-clipped 450 μm SCUBA-2 map.

the sources combined, however, the same single flux is given for both sources in Table 2. The splitting of the fluxes assumes that both sources are equally evolved. This assumption is supported by the similarity between the values of the mid-infrared spectral indices (at −0.86 and −0.78) for each source (see Section 4.3), as well as the consistency between each individual flux ratio (2.8 ± 0.1).

A further exception to the 850 μm 20 arcsec aperture sizes is given by the bright source in the NW field (L1YSO 7). Though this protostar was detected by *Spitzer* (as SSTc2d_J154301.3-340915), it clearly does not share the compact characteristics of the rest of the sources in this region. Therefore, an aperture of diameter 80 arcsec was used for this source, with a background flux annulus between 120 and 160 arcsec. The emission from this protostar extends far outside a 20 arcsec aperture, so the use of such a small aperture would have produced an inaccurate flux measurement.

The JCMT beam itself extends out beyond 20 arcsec, so apertures of this size will not pick up all flux associated with an unresolved source. Therefore, fluxes were multiplied by aperture correction factors depending on the size of the aperture used. These factors can be found in table 3 of Dempsey et al. (2013). This correction is done under the assumption that sources are point-like, so it would not be valid for an extended source (like L1YSO 7).

Photometry for all 15 sources, both detected and undetected, is given in Table 2. Where fluxes from SCUBA-2 were not available, upper limits were instead used. To calculate an upper limit for the flux of a source, each was modelled as a spherically symmetric Gaussian distribution of flux, $S(r) = S_0 e^{-r^2/2\alpha^2}$, where $\alpha = \mathrm{FWHM}/\sqrt{8\ln 2}$. The central peak flux values $S_0$ were set based on the noise levels in the map ($\sigma = 0.05$ mJy arcsec$^{-2}$ for the NW field and 0.06 mJy arcsec$^{-2}$ for the E and SW fields at 850 μm, $\sigma = 1.7$, 2.8 and 5.1 mJy arcsec$^{-2}$ for the NW, E and SW fields, respectively, at 450 μm). The noise level at the position of L1YSO 15, due to its proximity to the edge of the map, was higher than elsewhere with a value of 0.12 mJy arcsec$^{-2}$ at 850 μm. The FWHM of the Gaussian was set based on the size of the aperture used (20 arcsec in all cases where the source was not detected). To calculate the threshold for a 3$\sigma$ detection, the peak value was specified to this level. Total flux values were then calculated as the integral under the Gaussian within the aperture, modified by the aperture correction factors.

Where fluxes for YSOs were available at both 450 and 850 μm, a consistency check between the fluxes at each wavelength (assuming a fixed temperature) was performed using the relation

$$\frac{F_{450}}{F_{850}} = \left(\frac{\nu_{450}}{\nu_{850}}\right)^{\alpha}, \quad (1)$$

where $F$ denotes flux, $\nu$ denotes frequency and $\alpha = 2.8$ is an appropriate spectral index for discs (Buckle et al. 2015). For the three point-like sources detected at 450 μm (L1YSO 10, L1YSO 11 and L1YSO 14), the flux at 450 μm was predicted according to equation (1) using the flux obtained at 850 μm. Flux values were found to be consistent within 2$\sigma$.

In addition to the SCUBA-2 fluxes at 850 and 450 μm, flux measurements from the optical $B$ band to the millimetre regime at 1300 μm were compiled to construct SEDs for all YSOs (within the field of view of SCUBA-2) where data are available.

#### *4.1.2* Spitzer *Space Telescope*

The first additional data set used is that of the *Spitzer* observations used to set the positions of the YSOs. The observations carried out at 24, 70 and 160 μm with the MIPS (Rieke et al. 2004) are presented by Chapman et al. (2007). Resolution at 24, 70, and 160 μm is approximately 6, 18 and 40 arcsec, respectively. Additionally, observations at 3.6, 4.5, 5.8 and 8.0 μm with the IRAC (Fazio et al. 2004), and comparisons with the MIPS data, were carried out by Merín et al. (2008). Resolution at 3.6, 4.5, 5.8 and 8.0 μm is 1.6, 1.6, 1.8 and 1.9 arcsec, respectively.

A total of 17 candidate YSOs were identified by *Spitzer*, 13 of which are within the SCUBA-2 field of view. The full catalogue of YSOs can be found in the online data of Merín et al. (2008), with these data also being carried through to the compilation of Dunham et al. (2015). The *Spitzer* sources within the field of view of the SCUBA-2 maps in this publication are listed in Table 3.

**Table 3.** *Spitzer* photometry for YSOs in Lupus I, identified with IRAC and MIPS, from Merín et al. (2008). The source IRAS 15422-3414 (L1YSO 14) is also included, with IRAC and MIPS flux values as given in the original YSO candidate catalogue.

| ID | $S_{3.6}$ (mJy) | $S_{4.5}$ (mJy) | $S_{5.8}$ (mJy) | $S_{8.0}$ (mJy) | $S_{24}$ (mJy) | $S_{70}$ (mJy) | $S_{160}$ (mJy) |
|---|---|---|---|---|---|---|---|
| L1YSO 1 | 3.95 ± 0.40 | 2.76 ± 0.40 | 9.58 ± 0.75 | 42.70 ± 3.11 | 114.00 ± 11.20 | 2920.0 ± 279.0 | ... |
| L1YSO 2 | 0.49 ± 0.03 | 0.37 ± 0.03 | 0.35 ± 0.04 | 0.25 ± 0.06 | 0.41 ± 0.46 | ≤ 50.0 | ... |
| L1YSO 3 | 255.00 ± 14.30 | 225.00 ± 14.30 | 231.00 ± 12.50 | 284.00 ± 14.00 | 483.00 ± 44.60 | 468.00 ± 47.3 | ... |
| L1YSO 4 | 95.80 ± 4.98 | 81.50 ± 4.98 | 82.50 ± 3.99 | 100.00 ± 4.84 | 167.00 ± 15.50 | ≤ 50.0 | ... |
| L1YSO 5 | 2.18 ± 0.14 | 1.78 ± 0.14 | 3.52 ± 0.23 | 16.40 ± 0.92 | 56.10 ± 5.20 | 593.0 ± 56.2 | ... |
| L1YSO 6 | 178.00 ± 11.00 | 120.00 ± 11.00 | 99.80 ± 5.06 | 68.80 ± 3.28 | 13.00 ± 1.22 | ≤ 50.0 | ... |
| L1YSO 7 | ... | 25.20 ± 2.00 | 35.80 ± 3.00 | 118.00 ± 18.00 | 991 000.00 ± 99.00[1] | 154 00.0 ± 1540.0 | 57.2 ± 11.4[a] |
| L1YSO 8 | 5.48 ± 0.27 | 4.06 ± 0.27 | 3.29 ± 0.16 | 3.73 ± 0.18 | 3.44 ± 0.38 | ≤ 50.0 | ... |
| L1YSO 9 | 14.10 ± 0.68 | 15.40 ± 0.68 | 16.20 ± 0.77 | 19.10 ± 0.90 | 69.90 ± 6.46 | 204.0 ± 23.2 | ... |
| L1YSO 10 | 101.00 ± 5.12 | 104.00 ± 5.12 | 100.00 ± 4.73 | 94.30 ± 4.66 | 137.00 ± 12.70 | 702.0 ± 67.8 | ... |
| L1YSO 11 | 1580.00 ± 132.00 | 1420.00 ± 132.00 | 1690.00 ± 97.90 | 2170.00 ± 130.00 | 286.00 ± 270.00 | 4900.0 ± 459.0 | 52 000.0 ± 10 400.0 |
| L1YSO 12 | 111.00 ± 5.84 | 120.00 ± 5.84 | 94.60 ± 4.59 | 83.00 ± 4.12 | 100.00 ± 9.72 | 154.0 ± 20.1 | ... |
| L1YSO 13 | 37.70 ± 1.89 | 37.90 ± 1.89 | 35.80 ± 1.71 | 40.30 ± 1.91 | 38.50 ± 3.56 | ≤ 50.0 | ... |
| L1YSO 14 | 333.70 ± 26.30 | 323.0 ± 18.3 | 311.00 ± 17.10 | 255.3 ± 46.6 | 282.00 ± 26.20 | 296.00 ± 36.00 | ... |
| L1YSO 15 | ... | ... | ... | ... | ... | ... | ... |

*Note.* The full *Spitzer* YSO catalogue, including YSO classifications and fluxes/magnitudes from other surveys used, can be found in the online catalogue of Merín et al. (2008).
[a]These values are deemed unreliable in this analysis and hence are not used to produce the SEDs of this paper.

#### *4.1.3* Herschel

Bustamante et al. (2015) measure *Herschel* fluxes for four YSOs in Lupus I (L1YSOs 3, 4, 11 and 12). SPIRE fluxes at 250, 350 and 500 μm are of particular interest for this analysis. Fluxes at these wavelengths would help fill the sparse submillimetre regime of the SEDs. However the *Herschel* beam sizes, particularly at 500 μm, can be much larger than SCUBA-2s at 850 μm. Aperture sizes used in source photometry are also correspondingly larger (42 arcsec at 500 μm). These large apertures mean that there is significant contamination present in the *Herschel* fluxes from other structures near the YSOs. This effect is most pronounced for L1YSO 11, as the *Herschel* apertures encompass much of the structure identified as the cores L1S2s 3, 4 and 5 later in this paper. Hence, there is roughly an order of magnitude difference between the fluxes from *Herschel* at 500 μm and SCUBA-2 at 450 μm, respectively. This discrepancy means that a correction of the *Herschel* fluxes would be required for future analysis, when the complete census for all *Herschel* sources in Lupus I is published (Benedettini et al., in preparation). *Herschel* fluxes are thus not used in this paper.

#### *4.1.4 IRAS*

Two additional sources were detected by the IRAS (IRAS; Neugebauer et al. 1984). The first of these sources, IRAS 15422-3414, was detected by *Spitzer* (and hence fluxes were available for use in this paper) but was not presented in Merín et al. (2008). The second, IRAS 15435-3421, was outside the *Spitzer* field of view. IRAS fluxes from the point source catalogue, at 12, 25, 60 and 100 μm (Beichman et al. 1988) were used for these sources and others where available. The effective resolution of these IRAS bands is between 2 and 5 arcmin.

#### *4.1.5 AKARI*

Data from the AKARI mid-infrared all-sky survey (Murakami et al. 2007) are used where possible. AKARI observed with the InfraRed Camera (IRC; Onaka et al. 2007) in 9 and 18 μm bands, with a resolution of approximately 9 arcsec and with the Far-Infrared Surveyor (FIS; Kawada et al. 2007) in four bands at 65, 90, 140 and 160 μm, with an effective resolution of between 0.6 and 0.9 arcmin. IRC fluxes for sources in Lupus I can be found in Ishihara et al. (2010) and FIS fluxes are from Yamamura et al. (2010).

Table 4 lists the nine sources for which AKARI fluxes are available, along with the relevant identifiers. Source positions often differ slightly from those given in the *Spitzer* catalogues. Therefore, sources were matched by ensuring the given positions differed by less than the given accuracy of 2 arcsec (Ishihara et al. 2010) and that flux values appeared consistent with other surveys.

#### *4.1.6 WISE*

Magnitudes obtained from the *WISE* All-Sky Survey (Wright et al. 2010) were used for all 15 sources. *WISE* mapped the whole sky in four infrared bands. These bands (*W*1, *W*2, *W*3 and *W*4) have effective wavelengths of 3.4, 4.6, 12 and 22 μm, respectively. The effective resolutions of these bands are 6.1, 6.4, 6.5 and 12 arcsec, respectively. The magnitudes for all objects, including those in Lupus I, are listed in the *WISE* All-Sky Data Release (Cutri et al. 2012). *WISE* data were available across all bands for every one of these YSOs, further enhancing the level of sampling in the mid-infrared regime.

Table 5 cross-matches all *Spitzer* sources, as well as the additional IRAS sources, with sources from the *WISE* All-Sky Data Release (Cutri et al. 2012). Source positions are again not identical to those in the *Spitzer* catalogues, but they are usually well within the angular resolution of IRAC I (which has the highest diffraction-limited resolution value across both telescopes of 1.5 arcsec; Rieke et al. 2004). Noticeably, they do not match within 1.5 arcsec for the source IRAS 15398-3359. In Merín et al. (2008), the J2000 position of the bright, extended protostar (15:43:02.2-34:09:09) appears to have been confused with that of a nearby much fainter compact object (15:43:01.3-34:09:15). This object cannot be separately resolved from the protostar with e.g. SCUBA-2, but is visible in the IRAC 1 map.

**Table 4.** AKARI all-sky survey fluxes from Ishihara et al. (2010) and Yamamura et al. (2010) for YSOs within the SCUBA-2 field of view in Lupus I.

| ID | MIR ID[1] | $S_9$ (mJy) | $S_{18}$ (mJy) | FIS ID[a] | $S_{65}$ (mJy) | $S_{90}$ (mJy) | $S_{140}$ (mJy) | $S_{160}$ (mJy) |
|---|---|---|---|---|---|---|---|---|
| L1YSO 1 | 1538484-344036 | 160.6 ± 31.6 | ... | 1538486-344033 | 3261 ± 505 | 4603 ± 104 | 5360 ± 1720 | ≤ 4334 |
| L1YSO 3 | 1539278-344617 | 441.1 ± 28.6 | 521.5 ± 49.1 | 1539278-344616 | ≤ 854.3 | 602.7 ± 51.4 | ≤ 1164 | ≤ 5274 |
| L1YSO 5 | ... | ... | ... | 1542148-341020 | ≤ 933.9 | 986.8 ± 130 | ≤ 3701 | ≤ 492.3 |
| L1YSO 7 | 1543022-340907 | 110.5 ± 18.9 | 491.1 ± 37.1 | 1543019-340906 | 13 440 ± 642 | 26 260 ± 943 | 46 280 ± 6260 | 78 380 ± 3110 |
| L1YSO 10 | 1545088-341734 | 125.4 ± 25.4 | ... | ... | ... | ... | ... | ... |
| L1YSO 11 | 1545128-341730 | 2008 ± 14.2 | 2967 ± 26.7 | 1545123-341721 | 5554 ± 291 | 11 910 ± 176 | 30 280 ± 6780 | 54 130 ± 967 |
| L1YSO 12 | 1545174-341826 | 96.44 ± 2.79 | ... | ... | ... | ... | ... | ... |
| L1YSO 14 | 1545297-342339 | 256.7 ± 17.6 | 317.7 ± 13.6 | ... | ... | ... | ... | ... |
| L1YSO 15 | 1546447-343035 | 176.9 ± 42.5 | ... | ... | ... | ... | ... | ... |

*Note.* As with other surveys, fluxes for L1YSOs 3 and 4 are unresolved. They are listed in this table as given in the AKARI catalogues, under the ID of the brighter of the two sources. However, for the SED analysis, all were split according to the average flux ratio between the two sources for all IRAC and the MIPS 1 band.

[a]Multiple IDs are given to ensure clarity, including the separate IDs for AKARI mid-infrared (MIR) and far-infrared and submillimetre (FIS).

**Table 5.** *WISE* magnitudes for each YSO, in the four *WISE* bands (3.4, 4.6, 12 and 22 μm), taken from the *WISE* All-Sky Data Release (Cutri et al. 2012).

| ID | *WISE* ID | *W*1 (mag) | *W*2 (mag) | *W*3 (mag) | *W*4 (mag) |
|---|---|---|---|---|---|
| L1YSO 1 | J153848.37-344038.0 | 10.446 ± 0.022 | 10.111 ± 0.018 | 6.018 ± 0.014 | 4.044 ± 0.020 |
| L1YSO 2 | J153927.25-344844.2 | 14.811 ± 0.045 | 14.194 ± 0.059 | 11.509 ± 0.186 | 8.679 ± 0.338 |
| L1YSO 3 | J153927.75-344617.2 | 7.626 ± 0.028 | 7.178 ± 0.022 | 5.146 ± 0.015 | 3.193 ± 0.024 |
| L1YSO 4 | J153928.25-344618.1 | 8.579 ± 0.039 | 8.029 ± 0.034 | 6.312 ± 0.033 | 4.383 ± 0.066 |
| L1YSO 5 | J154214.56-341025.5 | 12.452 ± 0.023 | 11.998 ± 0.023 | 8.012 ± 0.023 | 5.302 ± 0.035 |
| L1YSO 6 | J154240.30-341342.8 | 8.006 ± 0.023 | 7.869 ± 0.020 | 7.385 ± 0.018 | 6.960 ± 0.096 |
| L1YSO 7 | J154302.21-340907.7 | 12.685 ± 0.023 | 8.872 ± 0.017 | 6.699 ± 0.018 | 2.371 ± 0.013 |
| L1YSO 8 | J154457.88-342339.4 | 11.891 ± 0.023 | 11.580 ± 0.022 | 9.798 ± 0.043 | 7.591 ± 0.128 |
| L1YSO 9 | J154506.33-341738.0 | 11.224 ± 0.023 | 10.233 ± 0.021 | 7.996 ± 0.020 | 5.126 ± 0.031 |
| L1YSO 10 | J154508.87-341733.6 | 8.864 ± 0.022 | 8.020 ± 0.020 | 6.339 ± 0.015 | 4.053 ± 0.022 |
| L1YSO 11 | J154512.84-341730.6 | 5.723 ± 0.054 | 4.973 ± 0.032 | 2.891 ± 0.010 | 0.856 ± 0.016 |
| L1YSO 12 | J154517.40-341828.4 | 8.440 ± 0.022 | 7.830 ± 0.018 | 6.510 ± 0.016 | 4.382 ± 0.023 |
| L1YSO 13 | J154518.51-342124.6 | 10.119 ± 0.022 | 9.464 ± 0.019 | 7.526 ± 0.018 | 5.738 ± 0.038 |
| L1YSO 14 | J154529.76-342338.9 | 7.769 ± 0.024 | 6.926 ± 0.019 | 5.429 ± 0.015 | 3.532 ± 0.019 |
| L1YSO 15 | J154644.72-343035.8 | 8.475 ± 0.023 | 8.046 ± 0.023 | 5.723 ± 0.015 | 3.680 ± 0.024 |

#### *4.1.7 Optical and near-infrared magnitudes*

Optical and near-infrared magnitudes are also used in the production of the YSO SEDs. The Two Micron All-Sky Survey (2MASS; Skrutskie et al. 2006) observed simultaneously in the *J*, *H* and *K* bands. Magnitudes for the sources in Lupus I are taken from Cutri et al. (2003). Comerón, Spezzi & López Martí (2009) presented imaging of Lupus I, III and IV undertaken with the Wide Field Imager (WFI) at the MPI-ESO 2.2 m telescope (Baade et al. 1999). Magnitudes in three bands ($R_c$, $I_c$ and $z_{\rm wfi}$) corresponding to 0.64, 0.79 and 0.96 μm, respectively, were obtained. *B* and *V* magnitudes used in this paper, corresponding to wavelengths centred around 0.44 and 0.55 μm, respectively, are taken from the Naval Observatory Merged Astrometric Dataset (NOMAD) catalogue (Zacharias et al. 2005).

#### *4.1.8 SEST*

Fluxes at 1300 μm, observed with the SEST (Booth et al. 1989), are taken from the independent observations of either Reipurth et al. (1993) or Nuernberger, Chini & Zinnecker (1997) when available. The effective resolution at 1300 μm is approximately 23 arcsec.

#### *4.1.9 Comparison between* Spitzer *and WISE fluxes*

As the IRAC 1, 2 and MIPS 1 detectors of *Spitzer* match closely in wavelength with *WISE* bands 1, 2 and 4, respectively (Werner et al. 2004; Wright et al. 2010), a comparison between the fluxes of *Spitzer* and the magnitudes of *WISE* enables an investigation of the consistency between these two surveys. To compare fluxes properly, *Spitzer* fluxes from IRAC 1, IRAC 2, IRAC 4 and MIPS 1 first had to be converted to magnitudes using equation (2). *Spitzer* zero-point reference fluxes for IRAC 1, 2 and 4 are 280.9 ± 4.1, 179.7 ± 2.6 and 64.13 ± 0.94 Jy, respectively (Reach et al. 2005). The zero-point flux for MIPS 1 is 7.17 ± 0.11 Jy (Rieke et al. 2008).

Once *Spitzer* fluxes were converted to magnitudes, the values needed to be modified to take into account differences, including in effective wavelengths, between the *Spitzer* and *WISE* filters. By interpolating between *Spitzer* bands, and providing corrective magnitude shifts, Antoniucci et al. (2014) produce relations to calculate effective *Spitzer* magnitudes at 3.4, 4.6 and 22 μm, i.e. corresponding to the effective wavelengths of the *WISE* 1, 2 and 4 bands.

IRAC 1 and MIPS 1 fluxes were not available for L1YSO 7, so the *Spitzer*–*WISE* comparison could not be made. Additionally, L1YSO 15 could not be compared as it was not observed by *Spitzer*. Thus, only 13 sources had their magnitudes compared.

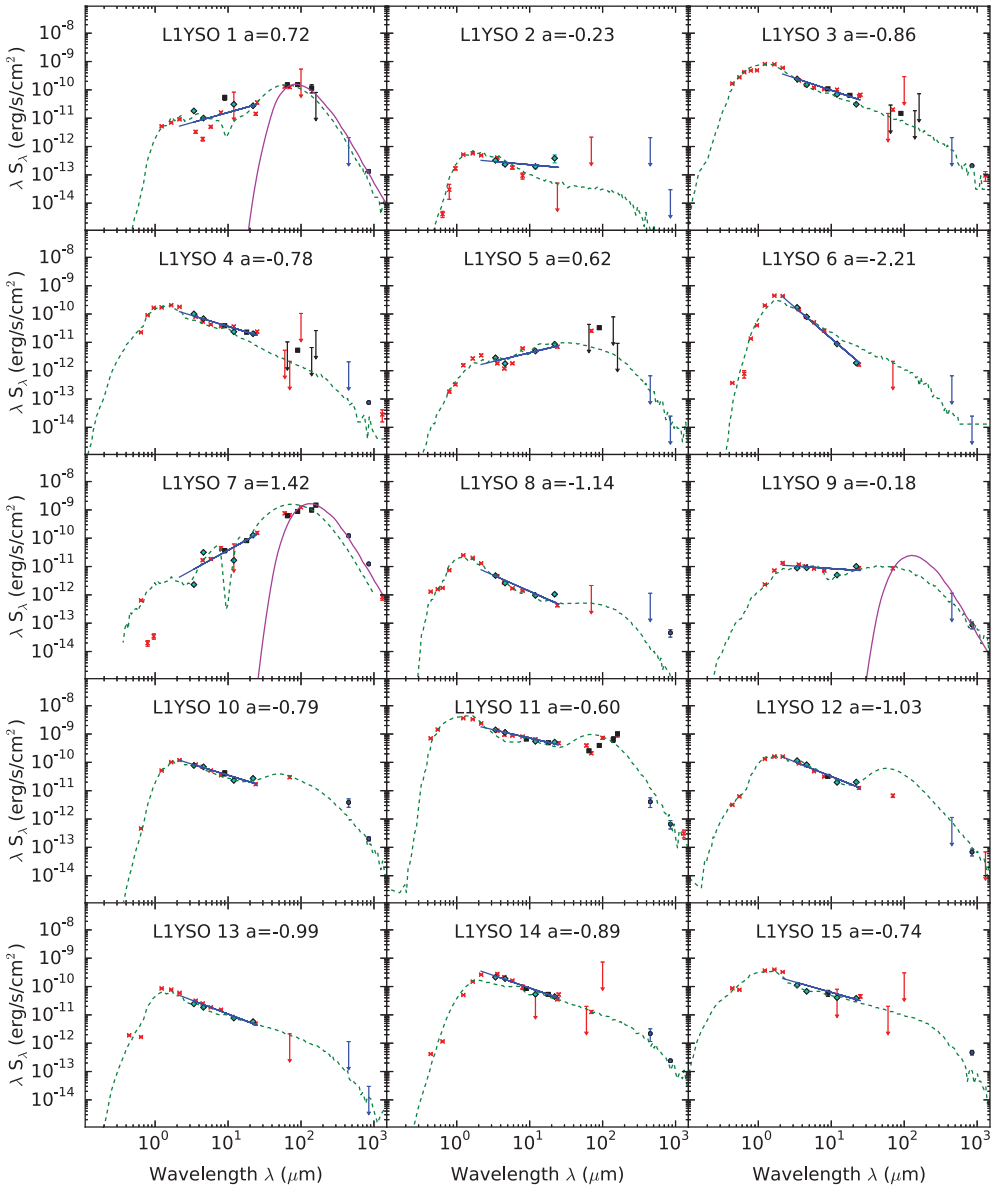


**Figure 4.** SEDs of all YSOs within the SCUBA-2 field of view (see Table 2) are presented here. Fits obtained using the models of Robitaille et al. (2006, 2007) are plotted as green dashed lines. Additionally, single temperature modified blackbody fits (Section 4.5) for protostellar envelopes are plotted as solid pink lines. SCUBA-2 data are plotted as solid blue circles, to distinguish them from the previously available data plotted as red crosses. Data from the AKARI mission (Ishihara et al. 2010; Yamamura et al. 2010), which were also not available for analysis by Merín et al. (2008), are plotted as black squares. The blue diamonds represent *WISE* fluxes (Cutri et al. 2012). Upper limits to fluxes are shown in the colours of their respective data sets. Values for the mid-infrared spectral index ($a$) are provided, and the slopes themselves are plotted as blue lines.

Effective *Spitzer* magnitudes for *W*1 and *W*2 for L1YSO 1 differ from the *WISE* magnitudes by approximately $6\sigma$. Antoniucci et al. (2014) perform a search for candidate eruptive variable protostars based on there being at least a $5\sigma$ difference. This difference would be significant as *Spitzer* and *WISE* observations were undertaken during different epochs, and variable stars observed this way would be expected to show a difference in brightness. In order to perform the comparisons, however, Antoniucci et al. (2014) specify that a source must not be flagged as extended in the *WISE* catalogue (Cutri et al. 2012). Since L1YSO 1 is flagged as extended, this analysis may not be valid for this YSO.

Another YSO, L1YSO 3, demonstrates a $5\sigma$ difference between magnitudes in the *W*4 band. Across the rest of the sources, average differences are much lower (less than $2\sigma$) and no other individual band has a difference approaching $5\sigma$. Therefore, values appear to be more consistent between *Spitzer* and *WISE* for most point-like, more evolved sources.

### 4.2 Spectral energy distributions

SEDs have been produced for each of the 15 YSOs in Lupus I, including all available literature fluxes for each source. The collation of these data allows for the fitting of model SEDs to each YSO. Also enabled for each source are the calculations of a mid-infrared spectral index, bolometric luminosity and bolometric temperature. SEDs for all sources, using observed fluxes (i.e. not extinction-corrected), are presented in Fig. 4.

**Table 6.** $B$, $V$, $R_c$, $I_c$, $z_c$, $J$, $H$ and $K$ bands, as well as *WISE* 1–4, shown with their corresponding central wavelengths and zero-magnitude reference fluxes.

| Band | Wavelength (μm) | Zero-mag reference flux (Jy) |
|---|---|---|
| $B^a$ | 0.44 | 4130 |
| $V^a$ | 0.55 | 3781 |
| ${R_c}^a$ | 0.64 | 3080 |
| ${I_c}^a$ | 0.79 | 2550 |
| ${z_{\rm wfi}}^b$ | 0.96 | 2450 |
| $J^c$ | 1.23 | 1594 |
| $H^c$ | 1.66 | 1024 |
| $K^c$ | 2.16 | 666.7 |
| $W1^d$ | 3.35 | 309.5 |
| $W2^d$ | 4.60 | 171.8 |
| $W3^d$ | 11.6 | 31.67 |
| $W4^d$ | 22.1 | 8.363 |

[a]Zero-magnitude reference fluxes from Bessell (1979).
[b]Waveband and zero-magnitude reference flux from Comerón et al. (2009).
[c]2MASS calibration from Cohen, Wheaton & Megeath (2003).
[d]*WISE* zero-magnitude reference fluxes from Jarrett et al. (2011).

In order to be plotted, data values originally given as magnitudes were converted to fluxes using the Pogson relation (Pogson 1856)

$$\frac{F_1}{F_2} = 2.512^{-(m_1-m_2)}, \tag{2}$$

where $F_1$ is the desired flux to be derived from the observed magnitude $m_1$. $F_2$ is the zero-magnitude reference flux for the particular band, and hence $m_2$ is, by definition, zero. Reference flux values used are given in Table 6. Table 6 also includes the custom $z$ band as defined in Comerón et al. (2009).

Where values from previous surveys were not available, the wavelength was simply not included in the SED. Upper limits for all sources in the c2d paper were also plotted as listed in Merín et al. (2008). For the two sources L1YSO 14 and L1YSO 15 that are not in the c2d paper, upper limits for IRAS fluxes are plotted as given in the IRAS point source catalogue (Beichman et al. 1988).

Similarly to *Herschel* (Section 4.1.3), IRAS and AKARI also have large beam sizes, and hence aperture photometry will suffer contamination from nearby structure if present, as it is with L1YSO 11. In particular, this aperture contamination provides an explanation for the strange shape of the SED for this YSO (seen in Fig. 4).

Where the beam at a certain wavelength large, it is also possible for multiple sources to fall within it. Therefore, certain fluxes may actually correspond to more than one YSO, resulting in a change in the shape of some SEDs. L1YSOs 3 and 4 are not resolved by SCUBA-2, while L1YSOs 9, 10 and 11 are in close proximity to each other, so their SEDs may be contaminated.

For L1YSO 7, MIPS 1 and MIPS 3 fluxes given in Merín et al. (2008) are inconsistent with all other fluxes from this source observed across multiple surveys. The MIPS 1 flux is almost two orders of magnitude greater than the MIPS 2 flux, while the MIPS 3 flux is over two orders of magnitude lower than the MIPS 2 flux. Hence, they have been excluded entirely from the SED analysis in this paper. The IRAS flux at 25 μm, the *WISE* magnitude at 22 μm, and the AKARI flux at 160 μm for this source mean that these areas of the spectrum are still reasonably well represented in the SED.

*Spitzer* data for the source L1YSO 14 is in fact available from the original YSO candidate catalogue. Though this source is still referred to by its IRAS name (and not by a preliminary *Spitzer* designation), these fluxes are used to help produce the SED for this YSO. These *Spitzer* fluxes appear to be consistent with those from IRAS and AKARI.

### 4.3 Spectral index

Once the data sets for each of the YSOs were collated, their evolutionary stages were estimated using the mid-infrared spectral index. First defined in Wilking, Lada & Young (1989) and expanded upon by Greene et al. (1994), the spectral index $a$ provides a measure of the 'slope' of the SED between 2.2 and 25 μm. The relation

$$a = \frac{d\log(\lambda F_\lambda)}{d\log\lambda}, \tag{3}$$

was calculated for each source using a linear least-squares fit to all available data between 2.2 μm ($K$ band) and 25 μm (IRAS 2). These values can be found in Table 7. Values for $a$ of $>0.3$ were used to classify a YSO as a Class I protostar and values of $-0.3 \geq a \geq -1.6$ resulted in a Class II classification, leaving values of $0.3 \geq a \geq -0.3$ to indicate a Flat-spectrum YSO (hereafter referred to as Class F). These Class F sources represent the evolutionary transition between envelope-dominated Class I sources and disc-dominated Class II sources. Any YSO with an $a$ value of $\leq -1.6$ was considered as Class III. Though not explicitly included in these calculations, a value of $a$ significantly greater than 0 can be indicative of a Class 0 protostar (André, Ward-Thompson & Barsony 1993; Enoch et al. 2009).

Spectral indices were calculated both for observed and extinction-corrected flux values. Fluxes were corrected using the extinction law of Robitaille et al. (2007, see also references therein). This extinction law was chosen to be consistent with the model fitting in Section 4.6.3. It does not differ substantially from the law of Weingartner & Draine (2001) used by Dunham et al. (2013) to calculate luminosities of *Spitzer* c2d-identified YSOs.

To perform these extinction corrections, a value for $A_{\rm v}$ was required for each YSO. Values found from the model fitting in Section 4.6.3 were preferred when that source was 'well fit' by the models (values given in Table 11). Where a YSO was not 'well fit,' $A_{\rm v}$ was assigned the same value as was used in Dunham et al. (2013). In the case where neither of these options was possible, the value obtained from the best-fitting model (directly output from the SED fitter) to each YSO was used (Section 4.6.3, Table 10). A best-fitting model was always available, but was not necessarily a good fit to the data (i.e. well fitting).

Of the 15 sources, three are Class 0/I, two are Class F/II (borderline), one is class III and the remaining nine are Class II sources. SCUBA-2 detected 11 of the 15 YSOs within the field of view at 850 μm, with the spectral indices that determine that two are Class 0/I, one is Class F and eight are Class II. Non-detections were not confined to more evolved YSOs, as missing YSOs encompass all spectral classes.

Of the 13 sources present in both Merín et al. (2008) and this work, 11 have the same classification in both. Note that the source L1YSO 2 is classified as Class F/II in this paper, and yet as Class III by Merín et al. (2008). New *WISE* data for L1YSO 2 have demonstrated increased emission at longer wavelengths (beyond 8 μm) and hence caused the source to be reclassified from Class III to an earlier type. Due to the lack of available long-wavelength fluxes, however, the evolutionary stage of this low-luminosity object is not certain.

**Table 7.** Calculated values of both observed and extinction corrected bolometric temperatures and luminosities for YSOs in Lupus I, along with spectral index $a$ values. Evolutionary Classes are specified, and values of extinction used in the corrections are provided.

| SSTc2d ID | $A_V$ | Observed | | | Corrected | | | YSO class |
|---|---|---|---|---|---|---|---|---|
| | | $L_{bol}$ ($L_\odot$) | $T_{bol}$ (K) | $a$ | $L_{bol}$ ($L_\odot$) | $T_{bol}$ (K) | $a$ | |
| L1YSO 1 | 0.05 | 0.42 | 130 | 0.78 | 0.42 | 130 | 0.81 | I |
| L1YSO 2 | 2.8 | 0.01 | 200 | − 0.23 | 0.01 | 300 | − 0.60 | F/II |
| L1YSO 3 | 1.0 | 1.4 | 2600 | − 0.86 | 2.0 | 3100 | − 0.88 | II |
| L1YSO 4 | 2.0 | 0.37 | 1900 | − 0.78 | 0.58 | 2400 | − 0.88 | II |
| L1YSO 5 | 2.9 | 0.10 | 140 | 0.62 | 0.11 | 180 | 0.53 | I |
| L1YSO 6 | 9.0 | 0.48 | 1860 | − 2.21 | 6.0 | 5700 | − 2.23 | III |
| L1YSO 7 | 2.9 | 2.3 | 55 | 1.42 | 2.4 | 58 | 1.45 | 0[a] |
| L1YSO 8 | 0.0 | 0.04 | 2100 | − 1.14 | 0.04 | 2100 | − 1.10 | II |
| L1YSO 9 | 5.7 | 0.05 | 580 | − 0.18 | 0.06 | 820 | − 0.32 | F/II |
| L1YSO 10 | 5.0 | 0.27 | 1160 | − 0.79 | 0.48 | 1700 | − 0.88 | II |
| L1YSO 11 | 1.4 | 8.6 | 2100 | − 0.60 | 12.4 | 3000 | − 0.60 | II |
| L1YSO 12 | 2.5 | 0.34 | 1800 | − 1.03 | 0.54 | 2400 | − 1.10 | II |
| L1YSO 13 | 2.3 | 0.14 | 2000 | − 0.99 | 0.22 | 2400 | − 1.10 | II |
| L1YSO 14 | 6.8 | 0.51 | 1140[b] | − 0.89 | 1.8 | 2300 | − 1.03 | II |
| L1YSO 15 | 0.8 | 0.75 | 2300[b] | − 0.74 | 1.1 | 2100 | − 0.74 | II |

*Note.* The presence of upper limits in the far-infrared and submillimetre regimes will serve to artificially lower $T_{bol}$ and similarly raise $L_{bol}$.
[a]The evolutionary Class for L1YSO 7 was clarified using $T_{bol}$.
[b]The large IRAS 100 μm upper limit would have served to artificially lower $T_{bol}$. Therefore, it was removed for these sources.

These numbers are similar, both in ratio and overall quantity, to those seen in the Ophiuchus north region. That cloud is near theupper Scorpius region of the Sco-Cen OB association just as Lupus I is near upper Centaurus-Lupus. In Ophiuchus N, Hatchell et al. (2012) find three Class 0, one Class F, seven Class II and one Class III sources, giving a total of 12 YSO candidates in the region, as part of a *Spitzer* c2d survey. The fraction of Class 0/I sources in both of these regions is much greater than for Lupus III, which has five Class I sources and 56 that are Class II. Additionally, Lupus III has approximately the same number of Class III as Class II objects (Merín et al. 2008). This difference suggests that Lupus I is a region with low-efficiency, ongoing star formation akin to Ophiuchus N, and in contrast to Lupus III (although the YSO sample sizes in Lupus I and Ophiuchus N are admittedly small).

The protostellar fraction for Lupus I (including Class 0, I and F) are also similar to those seen in the main Ophiuchus clouds, as well as Serpens (Dunham et al. 2015), although the total number of YSOs in these clouds is much higher. However, including the four additional YSOs in Merín et al. (2008) (one Class F, one Class II, and two Class IIIs), compared to the entire Dunham et al. (2015) catalogue of YSOs in the Gould Belt, the fraction of Class 0/I sources is proportionally higher (16 per cent versus11 per cent) in Lupus I. The fraction of Class II sources is lower, and with three Class III sources, giving a percentage of 16 per cent (compared to 40 per cent in the whole Gould Belt), the proportion of these more evolved YSOs is much lower. The ambiguity of L1YSO 2 means that it is difficult to say whether the number of Class F sources in Lupus I is typical or not.

The higher number of Class 0/I sources in Lupus I, and lower number of Class III YSOs, suggest that Lupus I is young. The ratio of Class 0/I to Class III sources in the SCUBA-2 map of Lupus I is 1:1, compared to 0.275 in the Dunham et al. (2015) catalogue. The apparent recent trigger for star formation is consistent with the hypothesis of Gaczkowski et al. (2015) that expanding shells from the Sco-Cen OB association have recently shocked Lupus I into a star-forming event. The number of YSOs in Lupus I (19) is low, so caution should be exercised with this result.

### 4.4 $L_{bol}$ and $T_{bol}$

The complete SEDs also allow us for calculations of a bolometric luminosity ($L_{bol}$) and bolometric temperature ($T_{bol}$) for each source. $L_{bol}$ is calculated by integrating flux $S_\nu$ over frequency:

$$L_{bol} = 4\pi d^2 \int S_\nu d\nu. \quad (4)$$

The bolometric temperature of a source is the temperature of a blackbody with the same flux-weighted mean frequency as the source SED (Myers & Ladd 1993), defined as

$$T_{bol} = 1.25 \times 10^{-11} \langle \nu \rangle \mathrm{K}, \quad (5)$$

where mean frequency $\langle \nu \rangle$ is defined as

$$\langle \nu \rangle = \frac{\int \nu S_\nu d\nu}{\int S_\nu d\nu}. \quad (6)$$

To calculate the integrals in equations (4) and (6), the trapezium rule was used to estimate the area under the SED, following Dunham et al. (2013). The trapezium rule was only used within the range of the data points, with no extrapolation outside these areas. Table 7 lists $L_{bol}$ and $T_{bol}$ for each of the YSOs in this paper. Values are calculated both from the observed fluxes of these YSOs, using the extinction correction detailed in Section 4.3. Extinction values used are through the cloud, rather than within the individual sources. $T_{bol}$ can be used to estimate the evolutionary stage of a YSO (Enoch et al. 2009). Classifications for the 15 sources, based on $T_{bol}$ values, largely agree with those derived from spectral indices. Spectral index values do not distinguish between Class 0 and Class I sources, but $T_{bol}$ can. Therefore, $T_{bol}$ is used to classify L1YSO 7 as a Class 0 protostar, and this is the Class given in Table 7.

10 of the YSOs in this paper are analysed by Dunham et al. (2015); L1YSOs 2, 7, 11, 14 and 15 were not. While it would at first appear that L1YSO 7 was analysed, the YSO at the relevant position has a very low luminosity, and a negative spectral index (−0.21). Therefore, it clearly does not correspond to the relatively bright Class 0 protostar, L1YSO 7. If there is indeed a smaller, more evolved source in close proximity to L1YSO 7, it may have provided a significant contribution towards the short-wavelength fluxes in the SED of this source.

Where the bolometric luminosities in this paper are not consistent with the Dunham et al. (2015) values, they are generally slightly higher. Similarly, the bolometric temperature values are often slightly lower. These differences are largely due to the inclusion of upper limits to fluxes in these calculations. For sources with several upper limits in the submillimetre regime, the true value will likely lie within the range between the calculations of this work and those of Dunham et al. (2015).

Uncertainties in the calculations of $L_{\rm bol}$ and $T_{\rm bol}$ can be very large, potentially over 50 per cent if there is no available data from MIPS 3 or AKARI at 160 μm (Enoch et al. 2009). Furthermore, Dunham et al. (2013) show that sources lacking far-infrared and submillimetre detections will have $L_{\rm bol}$ underestimated by an average of a factor of 2.5. Sources with such a gap in wavelength coverage include L1YSO 2 and L1YSO 15. Additionally, when upper limits are used, $L_{\rm bol}$ may be calculated as being much higher than in reality, and $T_{\rm bol}$ will be correspondingly too low. IRAS 100 μm upper limit values were not included in the calculations for L1YSOs 14 and 15 because the limits are very large and would have had an unacceptable effect on the derived values of $L_{\rm bol}$ and $T_{\rm bol}$.

Using the criterion of Di Francesco et al. (2007) that internal luminosity $L_{\rm int} < 0.1$ L$_\odot$, embedded (i.e. Class 0/I and potentially Class F) sources with $L_{\rm bol}$ below this value (where $L_{\rm bol} = L_{\rm int} + L_{\rm ext}$) must be very low luminosity objects (VeLLOs; see also Dunham & Vorobyov 2012). Two of the observed YSOs (2 and 9) are in this group, with another (L1YSO 5) at the border of the classification, having $L_{\rm bol} = 0.11$ L$_\odot$. L1YSOs 2 and 5 were among the four sources in total not detected by SCUBA-2 at either 450 or 850 μm (also including L1YSO 6 and L1YSO 13).

Protostellar sources may still be VeLLOs if $L_{\rm bol} > 0.1$ L$_\odot$ when their luminosities are dominated by the external component. This situation may arise, for example, due to heating by the interstellar radiation field (Dunham et al. 2008). Indeed, the high temperature derived in Section 4.5 (below) for L1YSO 1 indicates that it may also be a VeLLO. If so, then up to four Class 0, I and F YSOs in Lupus I would be VeLLOs, a much larger fraction than the 30 per cent found by Dunham et al. (2008).

L1YSO 11 (HT Lup) is the most luminous YSO, with $L_{\rm bol} = 12.4$ L$_\odot$. This is consistent with the value of $14.49^{+17.44}_{-6.23}$ L$_\odot$ from Prato, Greene & Simon (2003). Luminosities of the five YSOs (L1YSOs 3, 4, 11, 12 and 15) also analysed in Hughes et al. (1994) often differ between the two papers. The luminosity estimates of this paper should be more accurate, because they were made using a greater number of fluxes.

### 4.5 Opacity-modified blackbody SED envelope fitting

The main source of submillimetre emission for an early-type YSO (Class 0/I) is the dust envelope in which it is embedded (Adams, Lada & Shu 1987), with envelope contribution also likely to be significant for Class F sources. The spectral index calculations in Section 4.3 suggest a total of five YSOs in Lupus I are either Class 0, I or F, with only three of these detected by SCUBA-2.

For these three sources, L1YSOs 1, 7 and 9, a modified blackbody fit for the YSO envelope (at long wavelengths) was performed. Such a fit allows estimates of the temperatures and masses of cold protostellar envelopes.

Single temperature modified blackbody SEDs for each of the sources were produced by iterating over a grid of possible temperatures and masses. Each model was produced using the following relation:

$$S_\nu = \kappa_\nu \left(\frac{M}{d^2}\right) B_\nu(T, \nu). \quad (7)$$

$M/d^2$ is treated as a scaling factor ($N$), with $M$ corresponding to envelope mass and $d$ being the distance to Lupus I (182 pc). $B_\nu(T, \nu)$ is the Planck function with temperature $T$, and $\kappa_\nu$ is the opacity. Model 5 (thin ice mantles, gas density of $10^6$ cm$^{-3}$) from Ossenkopf & Henning (1994) was used to provide opacity values via linear interpolation. For each YSO, $B_\nu(T, \nu)$, $\kappa_\nu$, and consequently model flux, were evaluated at every wavelength corresponding to a data point longward of 60 μm. Where only upper limits to the flux were available, the data point was ignored for the purpose of fitting.

A probability was then calculated for each modified blackbody model. To calculate a likelihood for each model, $\chi^2$ was evaluated based on each data point and corresponding model flux. These likelihoods were then combined with simple priors on temperature and mass to produce final probability values.

The prior on mass was the same for all YSOs. Probability was zero outside the interval of $1 \times 10^{-4}$–50 M$_\odot$. Within this interval, $P(\log(M))$ was set to be flat, meaning that lower masses would be favoured over higher ones.

For L1YSOs 1 and 9, the temperature prior was set to be flat within the interval of 1–50 K, meaning that any temperatures within this range were considered to be equally probable.

A temperature for L1YSO 7 was calculated from the ratio of SCUBA-2 fluxes, assuming a full, opacity-modified Planck function (Reid & Wilson 2005) and a constant dust opacity spectral index, $\beta = 1.8$ (Hatchell et al. 2013). Following the method of Aniano et al. (2011), Pattle et al. (2015) and Rumble et al. (2016), a model beam convolution kernel was used to produce a map of dust temperature for the Class 0 protostar L1YSO 7. A mean dust temperature for L1YSO 7 was calculated to be $17 \pm 2$ K. This mean dust temperature was then used to provide a temperature prior for the model fitting, with probability (within the same temperature interval as the other YSOs) described by a Gaussian distribution. This function was centred at a temperature of 17 K, with a FWHM of 2 K.

Once probabilities were calculated for every model in the grid, mass and temperature were separately marginalized out to produce 1D probability distributions for temperature and mass, respectively. Final temperature and mass values are taken to be the most probable values (following the marginalisation), with uncertainties given as 95 per cent ($2\sigma$) confidence intervals. These values can be found in Table 8. Within the specified confidence limits, temperature and mass values are anticorrelated. The modified blackbody-derived temperature for L1YSO 7 of $19.2^{+0.6}_{-0.3}$ K is consistent with the value of $17 \pm 2$ K obtained from the dust temperature map. Modified blackbody SEDs corresponding to the most probable temperatures and masses for each YSO are plotted with the relevant SEDs in Fig. 4.

The envelope temperatures derived here, especially for L1YSO 1, are warmer (between ∼19 and 29 K) than might normally be expected. For example, Kirk, Johnstone & Di Francesco (2006) find that most submillimetre cores in the Perseus molecular cloud are fit by Bonner–Ebert spheres with temperatures between 10 and

**Table 8.** YSOs on which modified blackbody SED fits for the envelope were performed, and the values obtained for the temperatures and masses of the envelopes.

| ID | $T_{env}$ (K) | $M_{env}$ $10^{-3}$ ($M_\odot$) |
|---|---|---|
| L1YSO 1 | $28.8^{+1.9}_{-1.5}$ | $3.2^{+1.1}_{-0.9}$ |
| L1YSO 7 | $19.2^{+0.6}_{-0.3}$ | $350 \pm 60$ |
| L1YSO 9 | $20.1^{+4.4}_{-1.0}$ | $4.0^{+2.4}_{-3.3}$ |

19 K. In addition, Rumble et al. (2015) calculate a mean temperature of ∼15 K for YSOs in the Serpens MWC 297 region, also consistent with observations of the W40 complex (Rumble et al. 2016).

These higher temperatures, particularly for L1YSO 1, could be caused by the influence of the nearby Sco-Cen OB association, although Pattle et al. (2015) do not find such high temperatures in the nearby region of Ophiuchus. Gaczkowski et al. (2015) argue that Lupus I is affected by the interaction between an H I shell from upper Scorpius (de Geus 1992) and a wind bubble from upper Centaurus-Lupus. Such an interaction would have the potential to send shocks through the Lupus I molecular cloud.

The modified blackbody SED peak for L1YSO 1 lies at a shorter wavelength than seen with L1YSO 7, and this has led to the greater envelope temperature calculated by the fitting process. Further submillimetre data points (e.g. from *Herschel*) would clarify whether this 'early' peak is real. Similarly, L1YSO 9 has only two data points in the wavelength regime of the modified blackbody fitting process. Without more data points to fit, there is an increased range of temperatures and masses that produce a good fit to the data. Any future submillimetre observations of this YSO would improve the constraints provided by this fitting process.

At just a few Jupiter masses, the envelopes for L1YSOs 1 and 9 are not large. Given that L1YSO 9 is a Class F source, it would be expected that much of the protostellar envelope has already been accreted and/or dispersed. Therefore, a low envelope mass for this YSO is not surprising. It is possible that what is being seen here as an 'envelope' is actually partially or even wholly a circumstellar disc. The modified blackbody fits here are not able to distinguish between the two, but the models in Section 4.6.3 (below) are. The low envelope mass of L1YSO 1 is consistent with detection only being at a SNR of 2 at 850 μm, as a weak detection indicates a low amount of emitting dust particles. The mass for this YSO envelope is far below the brown dwarf limit, and may even be low enough for a sub-brown dwarf to be forming.

The envelope for L1YSO 7 is much more massive, at $0.35 \pm 0.06$ $M_\odot$. At a typical core to star efficiency of up to 40 per cent (André et al. 2010), this envelope mass suggests that this protostar may go on to form a low-mass star with a mass of approximately 0.15 $M_\odot$, or perhaps a multiple system with this total mass. Kristensen et al. (2012) used radiative transfer modelling in combination with observed submillimetre fluxes to find a mass for L1YSO 7 of 0.5 $M_\odot$, consistent well within a factor of 2.

### 4.6 Submillimetre YSO properties

#### 4.6.1 Protostellar envelopes

For the three sources that had modified blackbody fits performed, the masses as estimated from fitting (listed in Table 8) were preferred to those calculated from a single submillimetre flux. Therefore, these are the masses provided in Table 9. For the remaining two Class I/F YSOs (2 and 5), which were not detected by SCUBA-2, an upper limit to mass was calculated based on the upper limit to the flux at 850 μm (Table 3) using the relation

$$M = \frac{S_{850\,\mu m} d^2}{\kappa_{\nu(850\,\mu m)} B_{\nu(850\,\mu m)}(T)}, \quad (8)$$

adapted from Hildebrand (1983). Here, $S_{850\,\mu m}$ is the total flux density at 850 μm, $d$ is the distance to Lupus I ($182^{+7}_{-6}$ pc) and $B_{\nu(850\,\mu m)}(T)$ is the Planck function. $\kappa_{\nu(850\,\mu m)}$ is the dust opacity at 850 μm of 0.012 $cm^2\,g^{-1}$, consistent with both model 5 from Ossenkopf & Henning (1994) and the relation of Beckwith et al. (1990) ($\kappa_\nu = 0.1(\nu/10^{12}\,Hz)^\beta\,cm^2\,g^{-1}$) when dust spectral index $\beta = 2.0$. Note that a decrease in the value of $\beta$ would lead to smaller masses being calculated.

To calculate the value of the Planck function, a temperature of $15 \pm 2$ K, consistent with the YSO temperatures from Rumble et al. (2015), was assigned. Note that the assumption of larger temperatures leads to the determination of smaller masses and vice-versa. The calculated envelope mass limits for L1YSOs 2 and 5 are given in Table 9.

While the masses given in Table 9 for L1YSOs 1, 7 and 9 were estimated using modified blackbody fitting, the submillimetre (850 μm only) masses were also calculated. The same assumptions, given previously, were used as with the upper limits for L1YSOs 2 and 5. These values are provided, in parentheses, next to the modified blackbody-derived masses in Table 9. The 850 μm masses are larger than the modified blackbody masses, largely because the temperature assumed (15 K) is lower than found by the fitting.

**Table 9.** Envelope and/or disc masses for YSOs in Lupus I, calculated from 850 μm flux or modified blackbody fitting (where specified).

| SSTc2d ID | Envelope mass ($10^{-3}$ $M_\odot$) | Disc mass ($10^{-3}$ $M_\odot$) |
|---|---|---|
| L1YSO 1[b] | $3.2^{+1.1}_{-0.9}$ ($16 \pm 3$) | ... |
| L1YSO 2 | ≤3.6 | ≤0.9 |
| L1YSO 3 | ... | $7.5 \pm 0.8$[a] |
| L1YSO 4 | ... | $7.5 \pm 0.8$[a] |
| L1YSO 5 | ≤2.9 | ... |
| L1YSO 6 | ... | ≤ 0.8 |
| L1YSO 7[b] | $350 \pm 60$ ($1500 \pm 200$) | ... |
| L1YSO 8 | ... | $1.2 \pm 0.4$ |
| L1YSO 9[b] | $4.0^{+2.4}_{-3.3}$ ($11 \pm 3$) | $2.3 \pm 0.6$ |
| L1YSO 10 | ... | $5.3 \pm 0.9$ |
| L1YSO 11 | ... | $17 \pm 6$ |
| L1YSO 12 | ... | $1.8 \pm 0.5$ |
| L1YSO 13 | ... | ≤0.9 |
| L1YSO 14 | ... | $6.3 \pm 0.7$ |
| L1YSO 15 | ... | $12 \pm 2$ |

*Note.* Envelope masses are provided for Class 0, I and F YSOs, with disc masses being calculated for Class F, II and III YSOs. In reality, the masses for a Class F YSO would be expected to be a combination of the two values.
[a]These sources are not separately resolved by SCUBA-2, so the mass listed for both is the combined mass of the system.
[b]The envelope masses provided for these sources were calculated in Section 4.5. Values in parentheses were calculated from 850 μm flux.

#### 4.6.2 Disc sources

Typically, circumstellar discs will begin to be the main source of submillimetre continuum emission from YSOs once they reach later stages of evolution and become spectral Class II or Class III objects (Wilking et al. 1989). As previously mentioned, Class F YSOs are also likely to have a significant contribution to their submillimetre emission coming from a circumstellar disc. Spectral index values classify 12 YSOs in Lupus I as either Class F, II or III; nine of these disc sources are detected by SCUBA-2. Of these nine sources, there are eight distinct detections; the L1YSO 3/4 binary is unresolved by SCUBA-2.

The flux values obtained from the 850 μm data, given in Table 3, were used to calculate submillimetre continuum disc masses for these sources using equation (8). In this case, $T$ is assumed to be 20 K, in line with the work of Buckle et al. (2015) on the calculation of disc masses. The envelope temperatures calculated in Section 4.5 suggest that this dust disc temperature assumption may be too low, however. In general, more compact sources such as discs will be warmer than pre-stellar cores and protostars. Nevertheless, with the absence of hard evidence of higher disc temperatures, the standard value of $T = 20$ K was maintained. Should the temperature of these discs be higher in reality, this would lead to a reduction in the calculated disc masses. Moreover, disc temperature values will vary radially within the disc (e.g. Andrews & Williams 2005). Thus, disc masses calculated assuming a uniform temperature distribution should be treated as estimates.

Opacity is this time calculated assuming a $\beta$ value of 1.0 to account for more evolved dust around these YSOs (Beckwith & Sargent 1991). The evolution of dust from diffuse ISM to protostellar discs can alter grain properties. As $\beta$ is an optical property of dust grains, it can be expected to decrease with increasing grain growth (see Chen et al. 2016 and references therein). The effect of this change is a reduction in the calculated dust mass for compact sources as compared to more extended envelope structure. The calculated disc masses are listed in Table 9. When a source was not detected, an upper limit to the mass was instead calculated, based on the flux upper limits given in Table 2.

The distance used in this paper of $182^{+7}_{-6}$ pc is larger than some previous estimates of distance to the region (e.g. 155 ± 8 pc; Lombardi et al. 2008). Masses derived using a distance of 182 pc will be approximately 1.4 times greater than if a distance of 155 pc had been used.

Overall, the mean disc mass for the nine Class F and II YSOs detected by SCUBA-2 (the only Class III is not detected) is $5.9 \times 10^{-3}$ $M_\odot$, with values ranging over $1 - 17 \times 10^{-3}$ $M_\odot$. This is within a factor of 2 of the value of $4.5 \times 10^{-3}$ $M_\odot$ found by Buckle et al. (2015) in L 1495.

The source L1YSO 11 (with a disc mass of $17 \pm 6 \times 10^{-3}$ $M_\odot$) has a disc mass greater than the minimum mass Solar nebula (MMSN). This disc mass is consistent with the value of $15.5 \times 10^{-3}$. derived from 1300 μm flux by Nuernberger et al. (1997). This YSO is also the most luminous of the sample, with a bolometric luminosity of 12.4 $L_\odot$ (Table 7). This star is the Herbig Ae/Be star HT Lup (e.g. Kukarkin et al. 1971; Cutri et al. 2003) and demonstrates that one of the most massive and luminous stars in this low-mass region also has a potentially planet-forming disc of comparable mass to that of the young Solar system.

This single detection of a MMSN disc in Lupus I is consistent with the L1495 region of Taurus observed by Buckle et al. (2015). There, 20 YSOs were detected by SCUBA-2, and of these, two have disc masses (at $T = 20$ K) greater than the MMSN.

Additionally, L1YSO 15 has a disc mass of $12 \pm 2 \times 10^{-3}$ $M_\odot$. This matches the 1300 μm value of $12.2 \times 10^{-3}$ $M_\odot$ from Nuernberger et al. (1997) and means that this YSO also has a disc with a mass of approximately the MMSN. The binary of L1YSOs 3 and 4 is found to have a total disc mass of $7.5 \pm 0.8 \times 10^{-3}$ $M_\odot$, similar to the value of $6.4 \times 10^{-3}$ $M_\odot$ found by Nuernberger et al. (1997). This disc mass should be taken as an estimate for the combined disc mass of the system, acting as an upper bound for each individual YSO. As with its envelope mass in Section 4.6.1, the disc mass for the Flat-spectrum L1YSO 9 should be treated as upper limit. This YSO could be either a true protostar, or a disc obscured behind other extended material.

Following Buckle et al. (2015), disc masses were calculated from fluxes extracted at the literature positions of YSOs. Therefore, it is possible for smaller scale cloud structure to be misidentified as disc emission at known YSO locations. Positive emission is found near the position of L1YSO 8, but away from any YSO or core structure identified by SCUBA-2. Additionally, there is no obvious visual sign of a disc at this position in the SCUBA-2 maps. This means that the possibility of cloud structure contaminating disc signal for L1YSO 8 cannot be discounted. The detection of L1YSO 12 appears consistent with being faint disc emission, but again the potential contribution of ambient cloud signal is not entirely ruled out. It should be remembered, however, that the aperture photometry at these positions included a background subtraction (using an annulus) with the express purpose of removing ambient signal from the detection.

#### 4.6.3 Model SEDs

Robitaille et al. (2006) presented a grid of over 200 000 model SEDs computed via radiative transfer, which cover a wide range of disc and envelope masses as well as stages of evolution. A PYTHON fitting tool,[1] outlined in Robitaille et al. (2007), was used to fit models from the grid to the SED of each of the *Spitzer*-identified YSOs. The disc and envelope masses of well-fitting models were compared to those derived from the SCUBA-2 data (presented in Table 9), and constraints on interstellar extinction values for each YSO were sought. Furthermore, the fitting process revealed 'gaps' in the model grid, by finding SEDs which were not well fit by any models.

These models have been widely used to fit data in the mid-infrared regime (e.g. Simpson et al. 2012; Azimlu, Martínez-Galarza & Muench 2015) but fits involving submillimetre data have tended to focus on more distant, massive YSOs (e.g. Mottram et al. 2011; Faimali et al. 2012). Buckle et al. (2015) fit these models to data including SCUBA-2 fluxes but this is only performed on two YSOs. Moreover, for one of the YSOs, the model is a poor fit in the region of the SCUBA-2 data.

Convolved model fluxes were produced for each wavelength filter for which observed data were available. Many of these model fluxes were already available within the fitting tool, including *Spitzer*, 2MASS and IRAS. However, model fluxes had to be computed for the *WISE*, AKARI and SCUBA-2 filters. *WISE* filter profiles (Wright et al. 2010) are available online,[2] with wavelength and relative system response (RSR) provided. AKARI IRC filter profiles are shown in Onaka et al. (2007), with FIS profiles given in Kawada

[1] http://sedfitter.readthedocs.org/en/stable/
[2] http://wise2.ipac.caltech.edu/docs/release/prelim/expsup/

**Table 10.** *Spitzer*-identified YSOs, along with the additional IRAS sources, and their corresponding best-fitting models (Robitaille et al. 2006, 2007). Where possible, a best-fitting model is one that passed all tests and has the lowest $\chi^2$ value. Where no models for a particular YSO passed all tests, the best-fitting models from $\chi^2$ only are given. Values are given for the masses (from these models) of the YSO discs and envelopes.

| ID | Best-fitting model # | $\chi^{2\,a}$ | $M_{\rm disc}{}^{b}$ ($10^{-3}$ $M_\odot$) | $M_{\rm env}{}^{b}$ ($10^{-3}$ $M_\odot$) | $A_V$ |
|---|---|---|---|---|---|
| L1YSO 1 | 3015615_6 | 94.3 | 0.79 | 30 | 0.1 |
| L1YSO 2 | 3010945_1[c] | 19 | 0.82 | 0.19 | 2.8 |
| L1YSO 3 | 3013816_7[c] | 21 | 5.2 | ... | 2.1 |
| L1YSO 4 | 3009154_5[c] | 65 | 5.0 | ... | 1.3 |
| L1YSO 5 | 3006636_2[c] | 71 | 1.9 | ... | 2.7 |
| L1YSO 6 | 3014557_2[c] | 450 | 5.7 | ... | 6.1 |
| L1YSO 7 | 3010808_9[c] | 300 | 0.35 | 740 | 0.0 |
| L1YSO 8 | 3006431_4[c] | 62 | 0.64 | ... | 0.2 |
| L1YSO 9 | 3017650_2 | 27 | 11 | 0.42 | 2.1 |
| L1YSO 10 | 3007290_5 | 13 | 11 | 0.31 | 7.2 |
| L1YSO 11 | 3011911_9 | 290 | 84 | 84 | 1.4 |
| L1YSO 12 | 3010550_3 | 30 | 7.9 | 1.8 | 0.1 |
| L1YSO 13 | 3002284_10 | 93 | 2.2 | ... | 2.3 |
| L1YSO 14 | 3011667_5[c] | 220 | 21 | ... | 6.8 |
| L1YSO 15 | 3015916_10 | 81 | 7.8 | 0.31 | 0.6 |

[a] $\chi^2$ values are given per data point.
[b] Values are left blank if less than 0.01 Jupiter masses.
[c] Parameters should be considered unreliable, as these best-fitting models were not considered 'good' fits.

et al. (2007); RSRs for all filters are also available online.[3] SCUBA-2 filter profiles were available from the JCMT staff. It should be noted that in order to produce convolved flux files with the fitting tool, wavelengths in the input files must be in ascending order. This is not specified in the SED fitter documentation.

Data values, including uncertainties, were read in as fluxes, magnitudes or limits. Where a limit was used a confidence interval was specified, which for the fitting of these models was set to $3\sigma$ (99.7 per cent).

Extinction was also included in the fitting process, with a range of $0 \leq A_v \leq 7.39$. This range was chosen based on possible extinction values of up to the maximum value for Lupus I given in Cambrésy (1999). The range of possible distances was $182^{+7}_{-6}$ pc, consistent with the other analyses in this paper.

A selection of best-fitting models was initially found by minimizing $\chi^2$. For each YSO, every model with a $\chi^2$ per point value of less than 100 was initially selected. If no model fulfilled this criterion, then the overall best-fitting model for the YSO was still chosen, though parameters were not considered reliable. The best-fitting model SEDs for each source, according to the least-squares fitting process, are shown overplotted on the SEDs in Fig. 4. The exact model numbers for each source can be found in Table 10.

Once a selection of models satisfying the $\chi^2$ criterion was obtained, further statistical tests were run on them to exclude models that were not good fits, despite their (relatively) low $\chi^2$ value.

First, a Kolmogorov–Smirnov test was run on the residuals between the data and model fluxes at each filter's central wavelength. Convolved filter fluxes for each model were interpolated to correspond to the correct wavelength, and had distance and extinction corrections applied according to the values found in the fitting procedure. Residuals were fractional, with $R_\lambda = (S_{\rm data} - S_{\rm model})/S_{\rm model}$.

[3] http://svo2.cab.inta-csic.es/svo/theory/fps3/

**Table 11.** Parameters for the YSOs for which at least one model was well fit, along with the total number of these models. Parameters are given as the mean values across all well-fitting models.

| ID | $N_{\rm models}$ | $M_{\rm disc}$ ($10^{-3}$ $M_\odot$) | $M_{\rm env}$ ($10^{-3}$ $M_\odot$) | $A_V$ |
|---|---|---|---|---|
| L1YSO 1 | 1 | 0.79 | 30 | 0.05 |
| L1YSO 9 | 20 | 6.0 (0.01–45) | 4.8 (0.01–14.2) | $5.7 \pm 2.6$ |
| L1YSO 10 | 276 | 3.6 (0.01–70) | 36 (0.01–405) | $5.0 \pm 2.0$ |
| L1YSO 11 | 1 | 84 | 84 | 1.4 |
| L1YSO 12 | 53 | 6.8 (0.36–33) | 1.3 (0.01–10.6) | $2.5 \pm 1.5$ |
| L1YSO 13 | 5 | 2.2 (1.29–3.24) | 0.02 (0.01–0.04) | $2.3 \pm 0.5$ |
| L1YSO 15 | 2 | 9.6 (8.20–10.92) | <0.01 | $0.8 \pm 0.1$ |

*Note.* Uncertainties are only provided for extinction values, otherwise parameter ranges are shown in parentheses.

These fractional residuals were then normalized as $R_\lambda/R_{\rm rms}$, where $R_{\rm rms}$ is the rms of all residual values.

The distribution of normalized residuals was tested against a normal distribution with a mean of 0 and standard deviation of 1. For a model to be a good fit, any deviations between it and the data should be due to random fluctuations. Therefore, a failure to be consistent with a normal distribution is a mark of a poor fit. Consequently, a model was rejected if the distribution of normalized residuals failed a K–S test at the 10 per cent level.

An example of the utility of this test can be seen in the 'best-fitting' model of L1YSO 8, seen in Fig. 4. The $\chi^2$ per point value for this model's fit to the data is low, so it is not rejected initially. However, the model is substantially underestimating flux in the sub-millimetre regime (by more than an order of magnitude compared to the data at 850 μm). The strength of this deviation means that the model fluxes are very unlikely to have come from the same distribution as the data, therefore the K–S test enables this model, and others like it, to be rejected.

The second test was a Wald–Wolfowitz runs test. This tests explores whether a model can be rejected due to having too many model points above or below the data in sequence (a run). If a model is a good fit, the scatter of data points above and below the model values should be random. A very low number of runs is inconsistent with random scatter, and indicates that a model is not a good fit. Specifically, a model was considered to have failed the runs test if there was less than a 10 per cent chance of the observed number of runs being consistent with being drawn from a normal distribution about the expected number of runs.

After running these tests, a final set of well-fitting models was available for analysis (shown in Table 11). Overall, seven YSOs have at least one well-fitting model, and the remaining eight do not. Of the YSOs fit by well-fitting models, L1YSOs 1 and 11 are only well fit by one model. The remaining five YSOs (9, 10, 12, 13 and 15) are fit by more than one model, with L1YSO 10 fit by 276 models in total.

For YSOs with multiple well-fitting models, constraints on disc mass, envelope mass and extinction were sought. Extinction was constrained for all five of these YSOs, with the lowest extinction being found for L1YSO 15 ($A_v = 0.8 \pm 0.1$). Values for the other six YSOs, also detailed in Table 11, range between $A_v = 2.3$ and 5.7. Uncertainties in $A_v$, given in Table 11, are the standard deviation of extinction values from the mean for all well-fitting models. Uncertainties are only given when standard deviations are less than the mean value. The lower extinction for L1YSO 15 coincides with the relatively off-cloud location of this source; the other four YSOs lie on areas of extended emission visible on the 850 μm map.

Extinction values for the four well-fitting Class II sources (L1YSOs 10, 11, 12, and 13) are also provided by Merín et al. (2008). The extinction values derived from the model fitting are consistent with these values for YSOs 11, 12 and 13. The value calculated for L1YSO 10 is higher than that derived from the model fitting, at $A_v = 10.0$. However, the model fitting did not produce a higher extinction value for L1YSO 10 even when values of up to $A_v = 10.0$ were allowed.

Disc and envelope masses for the well-fitting models are also given in Table 11. Disc masses are constrained for L1YSOs 13 and 15, with values of $2.21 \pm 0.97$ and $9.56 \pm 1.36$ $M_{Jup}$, respectively. Both of these YSOs are only well fit by two models, whereas L1YSOs 9, 10 and 12 have many more corresponding fits. The groups of models for these three YSOs gives disc mass ranges of $<$0.01–45, 0.01–70 and 0.36–33 $\times 10^{-3}$ $M_\odot$, respectively.

Some disc masses are consistent with those calculated from the 850 μm data in Section 4.6.2, while others are not. Two Class II YSOs (13 and 15) do have constrained mass ranges from models. For L1YSO 13, the mean model disc mass is too large to be consistent with the model being a non-detection at 850 μm. For L1YSO 15, the range of $9.6 \pm 1.4 \times 10^{-3}$ $M_\odot$ is consistent with the value of $12 \pm 2 \times 10^{-3}$ $M_\odot$ derived from the SCUBA-2 data.

Envelope mass constraints for the Class II L1YSOs 13 and 15 indicate that if there is any envelope left, it should be very small ($\ll$1 Jupiter mass). For L1YSOs 9 (Class F), 10 (Class II) and 12 (Class II), there is again a spread of possible values from models, with envelope masses ranging between $<$0.01–0.14, $<$0.01–0.41 and $<$0.01 $M_\odot$, respectively. YSO 9 is classified as Class F, and could therefore still have a significant protostellar envelope. However, L1YSO 10 (Class II) apparently has the largest model envelope mass. This result suggests that while there are many well-fitting models for L1YSO 10, the fitting process is still unable to constrain the origin of fluxes in the submillimetre wavelength regime. It is unsurprising that uncertainties are large for these remnant envelopes, as they fall around or below the SCUBA-2 mass sensitivity limit of approximately $3.7 \times 10^{-3}$ $M_\odot$ at 182 pc (Holland et al. 2013).

A lack of constraint across both disc and envelope masses demonstrates that even for a single source, there can be significant variations in the properties of models that provide a 'good' fit to the data. It is therefore very difficult to derive reliable dust mass estimates from this SED fitting method alone. Spatial information on specific sources could help rule out some models. For example, a YSO observed as being a point source in Lupus I (at 182 pc) is unlikely to have a massive circumstellar envelope.

Furthermore, the envelope geometry of the models in the grid is dominated by free-fall rotational collapse. The resulting envelope structure may be less applicable to the outer regions of envelopes, where turbulence, magnetism and other conditions may be more important and which would be expected to show strong emission in the submillimetre regime. Also, the envelope models could be missing the colder, outer regions because of the way the outer radius is defined. In the models, the outer envelope radius can be at an absolute maximum four times the radius at which the optically thin radiative equilibrium temperature falls to 30 K. Often, however, it will be substantially less than this, being sampled from within the range of $4R_0$–$R_0/4$.

Although the model grid contains over 20 000 modelled YSOs (each at 10 inclinations), the observed SEDs for some sources are not realized in the grid. All but one model in the fitting of L1YSO 2 was unable to fit the data at all, suggesting gaps in the available models at this low-mass, low-luminosity extreme. Additionally, no model was able to fit the shorter wavelength fluxes of L1YSO 8, while still having a massive enough disc to produce the signal observed by SCUBA-2 at 850 μm. Such discrepancies are not exclusive to these two YSOs; rather, they provide effective examples.

A lack of models consistent with the SEDs of certain YSOs could also be caused by contamination in some of the larger beam fluxes (e.g. IRAS). In such a case, fluxes could contain signal not corresponding to the specific YSO in question. This would move the shape of the SED away from that of an isolated YSO, and therefore away from the SEDs in the model grid.

It is possible that L1YSO 8 is being fit very well. As mentioned in Section 4.6.2, 850 μm flux for L1YSO 8 may be being confused with or contaminated by ambient cloud emission. This would have the effect of increasing the submillimetre signal beyond that truly emitted by the underlying YSO.

Among the simply 'best-fitting' models for the YSOs, disc masses from the models are usually higher than those from single temperature fits. The models are able to characterize discs at multiple temperatures, which allows mass to be added at higher temperatures without significantly affecting the emission seen at 850 μm. It is also possible that variations in the dust model chosen (the SED models use a combination of Kim, Martin & Hendry 1994 and Whitney et al. 2003) and the value of the opacity spectral index $\beta$ have caused these discrepancies.

The exception to this is L1YSO 8. As previously discussed, the model fitting underestimates flux at long wavelengths for this source, leading to a corresponding decrease in dust mass. However, it should be noted that attempts to derive YSO dust masses from individual models are not the intended use of the SED fitter. In addition, the models were primarily created to constrain shorter wavelength data, with a reduced capacity to fit to submillimetre data.

The envelope mass of the best-fitting model to L1YSO 7 of 0.74 $M_\odot$ (as given in Table 10) is greater than the value of $0.35 \pm 0.06$ $M_\odot$ calculated from the modified blackbody SED fitting, but is still consistent within a factor of 2. L1YSO 9 was well fit by more than one model, with a mean envelope mass across all well-fitting models (Table 11) of $4.8 \times 10^{-3}$ $M_\odot$. Though this appears to be consistent with the 850 μm mass, the model envelope masses were spread over several orders or magnitude, so the mean is not a well-constrained quantity.

The envelope mass of the single well-fitting model for L1YSO 1 is, at $30 \times 10^{-3}$ $M_\odot$, too large to be consistent with the modified blackbody SED mass. The temperature of this source derived from the modified blackbody fitting is high ($\sim$29 K, Table 8). A decrease in this temperature (possible if e.g. the AKARI fluxes are unreliable) could increase the calculated mass value by enough to allow for consistency with the well-fitting model. Additionally, the main constraint on the envelope masses for L1YSO 1 is the SCUBA-2 850 μm flux, which is close to the detection limit and hence has correspondingly high uncertainties.

Forbrich et al. (2010) use the Robitaille et al. (2006) models to constrain protostellar evolutionary stages in the NGC 2264 and IC 348 clusters. Sources able to be fit by models with an envelope mass of less than $10^{-3}$ $M_\odot$ are considered to be Class II sources, rather than protostellar. Looking at the best-fitting models for the Lupus I YSOs in Table 10, the envelope mass of L1YSO 9 ($0.42 \times 10^{-3}$ $M_\odot$) lies below this threshold. However, there is a degeneracy between models which fit the SED. The average mass across all well-fitting models for this YSO is large enough for this source to be considered protostellar. Moreover, an envelope mass of 0.084 $M_\odot$ is predicted for the Class II source L1YSO 11. This may be an effect of the

aperture contamination from nearby extended emission discussed in Section 4.2. All envelope sources are small enough that they will not be affected by spatial filtering in the SCUBA-2 data reduction, as none are larger than 2.5 arcmin.

### 4.7 Star formation rate

A previous estimate of the star formation rate (SFR) in Lupus I was $3.25 \pm 1.8$ $M_\odot$ $Myr^{-1}$ (Heiderman et al. 2010). This SFR has been updated based on a revised YSO count and recent mass and lifetime estimates. For example, Gaczkowski et al. (2015) derive masses specifically for B228 (the main filamentary ridge of Lupus I) from *Planck*, *Herschel* and Large APEX Bolometer Camera (LABOCA; Siringo et al. 2009) observations of ∼170 $M_\odot$. This mass is modified to $250 \pm 20$ $M_\odot$ due to the assumed distance in this work of 182 pc.

Galli et al. (2015) find an average disc lifetime in Lupus (specifically for Classical T-Tauri Stars, CTTS, before they transition to Weak-line T-Tauri Stars) of $3 \times 10^6 (M_\star/M_\odot)^{0.55 \pm 0.1}$ yr. Assuming an average stellar mass of $0.5 \pm 0.1$ $M_\odot$ as used by Heiderman et al. (2010) (consistent with the initial mass function of Chabrier 2003 and constrained by the mass distribution of YSOs observed by *Spitzer* in Spezzi et al. 2008), an average lifetime of $2.1 \pm 0.3$ Myr is expected.

A total of 11 *Spitzer* YSOs lie within the LABOCA field of view (B228). Adding L1YSOs 14 and 15 to this number means that there are a total of 13 known YSOs on the ridge. Of these YSOs, 11 are Class II (CTTS) or Class F. Therefore, the SFR for B228, using these updated quantities, is $2.6 \pm 0.6$ $M_\odot$ $Myr^{-1}$.

Compared to the SFRs in Heiderman et al. (2010), this represents a lower SFR than is seen in Lupus III, V and VI, but it is similar to the SFR of Lupus IV. Chamaeleon I is similarly massive to Lupus I, but has a higher SFR ($22.2 \pm 12$ $M_\odot$ $Myr^{-1}$).

More massive regions, such as Ophiuchus ($72.5 \pm 39$ $M_\odot$ $Myr^{-1}$) and Perseus ($96.2 \pm 52$ $M_\odot$ $Myr^{-1}$), have much higher SFRs. However, Chamaeleon III, which is more massive than Lupus I, has a lower SFR of $1.00 \pm 0.54$ $M_\odot$ $Myr^{-1}$.

Overall, this indicates that while the SFR of Lupus I is fairly low compared to other Gould Belt clouds, it is not low enough so as to be unusual.

Using the age of the oldest YSO in B228 for which an age has been calculated ($3.16 \pm 1.09 \times 10^6$ yr for L1YSO 15; Hughes et al. 1994) as an approximator of cloud lifetime, this then gives a star formation efficiency of $3.3 \pm 1.4$ per cent. Note that this is the efficiency of the main ridge of Lupus I, and not the entire cloud.

## 5 CORES

So far, this work has focused on the YSOs of Lupus I. The extended submillimetre structures in the cloud, including starless, pre-stellar and protostellar cores, are examined in the following analyses.

### 5.1 Identification and masses

#### *5.1.1 Core extraction*

The Starlink CUPID package (Berry et al. 2013) allows us for the identification of extended cores in SCUBA-2 dust continuum emission maps. In order to identify the bounds of extended objects within the Lupus I map, the FellWalker algorithm (Berry 2015) was used. This method treats cores as individual areas of emission that share a common significant peak. For a separate core to be identified, it must contain emission at a minimum specified value that can act as the peak. The FellWalker algorithm has been used previously by Rumble et al. (2015) for the identification and characterization of cores in the Serpens MWC 297 region, and Kirk et al. (2016) in Orion B.

FellWalker is a gradient-tracing algorithm; it proceeds iteratively from a low value in the map up to a peak data value. For the identification of cores in the 850 μm map of Lupus I, the low value was specified to be a pixel (9 $arcsec^2$) at a level of at least 0.12 mJy $arcsec^{-2}$ ($2\sigma$ rms in the E and SW field and $2.4\sigma$ in the NW field). Peaks had to have a minimum value of 0.3 mJy $arcsec^{-2}$ (i.e. a $5\sigma$ detection in the SW and E fields and $6\sigma$ in the NW field) for them to be considered as the central point of a core. Any emission at a level lower than 0.12 mJy $arcsec^{-2}$ was not considered as part of a core and was ignored.

Additionally, for pixels to be considered as part of a core, it was specified that they must be within 4 pixels of a pixel already included in a core-like structure. To avoid noisy pixels and prevent undesired levels of fragmentation, a minimum core size of 15 pixels was enforced, corresponding to a size of 135 $arcsec^2$. Overall, the non-default parameters used were: 'MaxJump = 4', 'MinDip = 0.12', 'Minheight = 0.3', 'MinPix = 15', 'FwhmBeam = 2' and 'MaxBad = 0.5'.

All pixels considered as part of the same core were assigned the same index value within a data mask, starting at one for the first area identified by the algorithm. Candidates located in the PONG edge regions of the map, where local noise is higher than the global noise used in FellWalker, were rejected by visual inspection. This strategy left a total of 14 separate objects corresponding to true signal. Some of these, identified in relative isolation, are disc detections corresponding with the aperture photometry measurements already taken. Therefore, two objects were excluded on the basis that they had already been identified, characterized and analysed as disc-like sources (the unresolved binary of L1YSOs 3 and 4, and L1YSO 15). Both are isolated point sources, with no extended structure evident.

To extract flux for the 12 identified cores at 450 μm, the core boundaries calculated for the 850 μm map were transposed over to the 450 μm map, and the flux within the boundaries of each identified core was measured. The position of the peak at 850 μm was used as the sky position of the core. The total flux of the core was then the sum of the flux at each pixel marked as part of the core footprint. Uncertainties were calculated assuming an error of 1 $\sigma_{\rm rms}$ per pixel. Consistency between the 450 and 850 μm fluxes (see Table 13) was checked using the relation

$$\frac{S_{450}}{S_{850}} = \frac{B_{450}(T)}{B_{850}(T)} \left(\frac{850}{450}\right)^{\beta}, \quad (9)$$

where the temperatures used are detailed in Section 5.1.2, and can be found in Table 12. All fluxes were found to be consistent (within uncertainties), provided that the cores L1S2 3, L1S2 4 and L1S2 5 are treated as a single agglomeration.

The 12 cores are presented in Table 13, with Fig. 5 showing the positions of each of these sources. $3\sigma$ upper limits for L1S2 11 and L1S2 12 were calculated at 450 μm using the same method used for point sources in Section 4.1.1. Sources were treated as Gaussian distributions of flux, with a peak emission at $5\sigma$. The FWHM assumed for each core was set to twice the core radius. Core radii were calculated from the number of pixels comprising the core area, and were not deconvolved.

The assumption of cores as spherical (in order to calculate radii and volumes) provides consistency with the work of Rumble et al. (2015), which also used FellWalker. Cores can, however, be elongated rather than spherical (seen with L1S2 2 and L1S2

**Table 12.** Correspondences between cores identified by SCUBA-2 (this work) and LABOCA (Gaczkowski et al. 2015). The 870 μm masses are provided, as well as the temperatures used in calculating core masses from SCUBA-2 fluxes (discussion in the text).

| Core ID SCUBA-2 | Core ID LABOCA | $M_{870}$ ($M_\odot$) | $M_{850}$ ($M_\odot$) | $T$ (K) | Field |
|---|---|---|---|---|---|
| L1S2 1 | 1 | 1.71 | 1.69 ± 0.40 | 15.5 ± 3.6[a] | NW |
| L1S2 2 | 2, 5 | 2.05 | 2.99 ± 0.85 | 12.8 ± 3.6 | E |
| L1S2 3, 4, 5 | 3, 4 | 0.67 | 0.90 ± 0.15 | 15.0 ± 3.0 | E |
| L1S2 6 | ... | ... | 0.18 ± 0.05 | 14.0 ± 3.0[b] | E |
| L1S2 7 | 6, 7, 8, 9, 10 | 2.61 | 2.11 ± 0.44 | 13.0 ± 2.6 | NW |
| L1S2 8 | 11 | 0.53 | 0.21 ± 0.05 | 13.5 ± 2.7 | E |
| L1S2 9 | ... | ... | 0.17 ± 0.05 | 14.0 ± 3.0[b] | E |
| L1S2 10 | ... | ... | 0.25 ± 0.06 | 14.0 ± 3.0[b] | E |
| L1S2 11 | ... | ... | 0.16 ± 0.04 | 14.0 ± 3.0[b] | SW |
| L1S2 12 | ... | ... | 0.07 ± 0.02 | 14.0 ± 3.0[b] | SW |

*Note.* Uncertainties on LABOCA masses are conservatively 20 per cent per core.
[a]Mean of both SCUBA-2 and *Herschel* temperatures.
[b]Temperatures are the mean of LABOCA core temperatures within the SCUBA-2 field of view.

**Table 13.** Protostar and pre-stellar core properties derived from SCUBA-2 continuum data (discussion in the text).

| ID | JCMTLSG name | $S_{450}$ (mJy) | $S_{850}$ (mJy) | $M_{850}$ ($M_\odot$) | Radius (arcsec) | $M_{\rm Jeans}$[a] ($M_\odot$) | $M_{850}/M_{\rm Jeans}$ | $M_{\rm Virial}$ ($M_\odot$) | $\alpha_{\rm vir}$ |
|---|---|---|---|---|---|---|---|---|---|
| L1S2 1 | J154301.6-340909 | 24 400 ± 200 | 4176 ± 9 | 1.69 ± 0.40 | 45 | 1.0 ± 0.2 | 1.7 ± 0.6 | 4.3 ± 0.6 | 2.6 ± 0.7 |
| L1S2 2 | J154500.6-341718 | 23 800 ± 300 | 5302 ± 9 | 2.99 ± 0.85 | 61 | 1.1 ± 0.3 | 2.7 ± 1.1 | 3.3 ± 0.6 | 1.1 ± 0.4 |
| L1S2 3 | J154513.4-341702 | 5890 ± 200 | 833 ± 6 | 0.36 ± 0.08 | 26 | 0.6 ± 0.1 | 0.6 ± 0.2 | ... | ... |
| L1S2 4 | J154512.7-341727 | 1220 ± 160 | 317 ± 5 | 0.14 ± 0.03 | 16 | 0.3 ± 0.1 | 0.4 ± 0.1 | ... | ... |
| L1S2 5 | J154516.8-341710 | 4470 ± 210 | 932 ± 7 | 0.40 ± 0.09 | 28 | 0.6 ± 0.1 | 0.7 ± 0.2 | 3.9 ± 0.4 | 9.8 ± 2.4 |
| L1S2 6 | J154529.2-342335 | 2250 ± 170 | 365 ± 5 | 0.18 ± 0.05 | 21 | 0.4 ± 0.1 | 0.4 ± 0.1 | 1.5 ± 0.2 | 8.4 ± 2.6 |
| L1S2 7 | J154249.8-340805 | 18 300 ± 200 | 3856 ± 10 | 2.11 ± 0.44 | 64 | 1.2 ± 0.3 | 1.8 ± 0.5 | 11.6 ± 1.4 | 5.5 ± 1.3 |
| L1S2 8 | J154525.8-342346 | 3220 ± 170 | 408 ± 5 | 0.21 ± 0.05 | 22 | 0.4 ± 0.1 | 0.5 ± 0.2 | ... | ... |
| L1S2 9 | J154508.7-341718 | 1930 ± 170 | 358 ± 5 | 0.17 ± 0.05 | 21 | 0.4 ± 0.1 | 0.4 ± 0.1 | ... | ... |
| L1S2 10 | J154527.1-342256 | 3860 ± 180 | 514 ± 6 | 0.25 ± 0.06 | 25 | 0.5 ± 0.1 | 0.5 ± 0.2 | ... | ... |
| L1S2 11 | J154035.0-344022 | ≤ 430 | 328 ± 5 | 0.16 ± 0.04 | 21 | 0.4 ± 0.1 | 0.4 ± 0.1 | ... | ... |
| L1S2 12 | J153934.5-344556 | ≤ 320 | 153 ± 3 | 0.07 ± 0.02 | 15 | 0.3 ± 0.1 | 0.2 ± 0.1 | ... | ... |

*Notes.* Uncertainties from flux calibration, not included in the table, are 4.84 per cent and 13.6 per cent at 850 and 450 μm, respectively (Dempsey et al. 2013). Core radii are not deconvolved.
[a]Although not quantified, volumes being treated as spherical will lead to additional uncertainties in the Jeans mass.

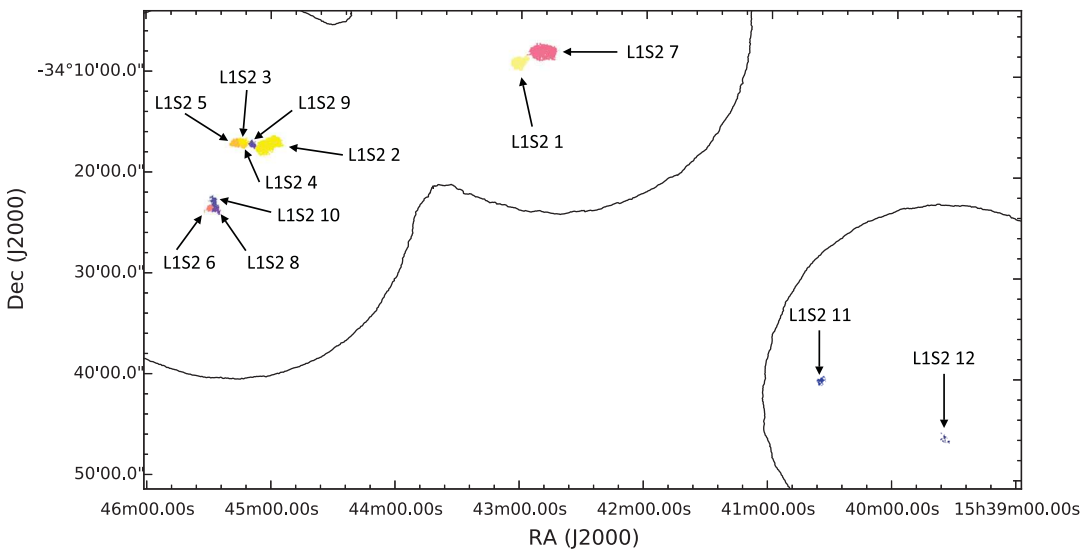


**Figure 5.** Protostars and pre-stellar cores (see Table 13) identified from the SCUBA-2 850 μm map of Lupus I using FellWalker (Berry 2015). Black contours show the edge of the SCUBA-2 coverage.

7). In this case, the effective radius of a core will be a lower limit if the third dimension is elongated, and an upper limit if the third dimension is shortened.

### 5.1.2 Core masses

The submillimetre continuum derived masses for these cores were calculated using equation (8) and the extracted submillimetre flux at 850 μm. The same value for the dust opacity of 0.012 $cm^2$ $g^{-1}$ was used for these cores as was used for the protostellar envelope calculations in Section 4.6.1. This is again consistent with both model 5 of Ossenkopf & Henning (1994) and the relation of Beckwith et al. (1990) when $\beta = 2.0$.

The observations of Gaczkowski et al. (2015) identified a total of 15 pre-stellar, protostellar and starless cores, in the main ridge of Lupus I, with LABOCA. They also derive temperatures for each of these cores by using *Herschel* SPIRE (Griffin et al. 2010) observations to create temperature maps. The correspondence between SCUBA-2 and LABOCA cores is shown in Table 12.

Where there is a match in position between LABOCA and SCUBA-2 cores, these derived temperatures are used in equation (8) in order to calculate the value of the Planck function. In the cases where a SCUBA-2 core corresponds to multiple LABOCA cores, the temperature used is the mean value across all relevant LABOCA cores. Moreover, where a SCUBA-2 core has no corresponding LABOCA object, the mean temperature value across all LABOCA cores (within the SCUBA-2 field of view) of 14 ± 3 K is used as an estimate.

The core L1S2 1 corresponds to the YSO L1YSO 7. Therefore, two temperatures were available to use for this source (from *Herschel* and SCUBA-2 in Section 4.5). The SCUBA-2-derived temperature value applies to a smaller scale (i.e. has better resolution) than the *Herschel* temperature, because the longest wavelength SCUBA-2 resolution is superior to the longest wavelength *Herschel* resolution. The identified FellWalker core has a higher flux value than was extracted for L1YSO 7 from aperture photometry as it covers a wider area of extended emission. Therefore, the temperature used to calculate the mass for L1S2 1 is the mean of the *Herschel* and SCUBA-2 values (14.0 and 17 K, respectively).

The mass–size relationship for these cores is plotted in Fig. 6. The cores with the largest radii are also the most massive. Core mass can be modelled simply as $M = 2\pi\Sigma_m r^2$, with $\Sigma_m$ the mean mass per unit surface area. Therefore, a core with a larger radius will be more massive provided $\Sigma_m \sim r^{-\gamma}$, where $\gamma < 2$. For these cores, $\Sigma$ is uncorrelated with the mean core radius, meaning that $\gamma \sim 0$ and the largest cores will indeed be the most massive. Also visible in this figure is the cluster of cores at similar sizes/radii. The majority of the cores identified range between 0.1 and 0.4 $M_\odot$ in mass, and ∼3000–5000 au in size (corresponding to approximately 1–2 beam FWHM at 850 μm).

Of the 12 extended sources, three have $M > 1.0$ $M_\odot$, eight have masses between 0.1 and 1.0 $M_\odot$ and one has a mass below 0.1 $M_\odot$. The total mass of all cores is 8.7 $M_\odot$, with a mean mass of the cores seen with SCUBA-2 of 0.73 $M_\odot$. Assuming a typical core-to-star mass efficiency of 40 per cent, star formation possibilities include low-mass stars (a maximum of ∼1 $M_\odot$ from L1S2 2) and brown dwarfs, assuming core collapse proceeds in the first place.

### 5.1.3 Comparison with LABOCA 870 μm observations

The most clustered region in Lupus I is at the SE part of the ridge, known in this paper as the E field. In this region, eight cores were identified by SCUBA-2 and six by LABOCA. In addition, two cores were identified by SCUBA-2 in the area of the N field. In contrast, LABOCA identified eight cores in this region. Further cores were identified in both analyses, but these were not in areas with shared coverage. SCUBA-2 cores were identified by FellWalker, and LABOCA cores were identified using CLUMPFIND (Williams, de Geus & Blitz 1994).

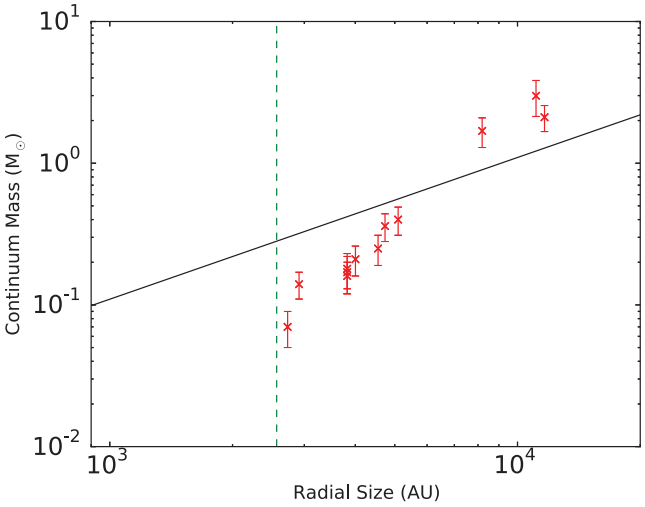


**Figure 6.** Masses of protostars and pre-stellar cores in Lupus I identified with the FellWalker algorithm (Berry 2015) and their radii. The solid black line represents the Jeans mass for given sizes, assuming a temperature of 14 K, and a $\beta$ value of 1.8). The green dashed line represents the JCMT beam size (14.1 arcsec at 850 μm).

Of the seven SCUBA-2 identified cores for which there is a corresponding LABOCA core, the continuum masses are consistent between all but one of them, once uncertainties are taken into account. The mass of L1S2 8 is significantly lower than the corresponding LABOCA core (0.21 versus 0.53 $M_\odot$). Both SCUBA-2 and LABOCA masses for corresponding cores are given in Table 12.

The LABOCA cores all have larger given sizes than the SCUBA-2 cores, and fluxes are also larger, with the exception of Core 1 (L1S2 1). The LABOCA beam size (21.2 arcsec) is larger than the SCUBA-2 beam size (14.1 arcsec). Additionally, the LABOCA observations exhibit superior recovery of faint, large-scale emission found in the regions around cores. This enables LABOCA cores to have a larger extent, and consequently produce a greater flux detection than the SCUBA-2 cores. L1S2 7 also has an extent greater than 2.5 arcmin along one axis, meaning that it may be affected by the spatial filtering in the SCUBA-2 data reduction. The effect of this would be an underestimation of both the flux and size of the core.

The presence of YSOs near or within certain cores (e.g. L1YSO 11 is coincident with L1S2 4) means that $T$ and $\beta$ will likely not be uniform across all of these structures. Treating all emission as extended (with $\beta = 2.0$ and $T < 20$ K) is therefore likely to lead to an overestimation of masses in these cores.

CLUMPFIND uses contours in the data to identify clumps of emission, but noise spikes in the data (corresponding to a single 'real' core) can lead to several separate clumps being identified (see Berry 2015 and references therein). FellWalker would be expected to avoid this problem, thus providing a possible explanation for the identification of L1S2 7 as five separate LABOCA cores (6, 7, 8, 9, 10). There is no clear visual indication in the SCUBA-2 map of significant substructure in L1S2 7 corresponding to the locations of the LABOCA cores. If, however, L1S2 7 does in fact consist of

**Table 14.** List of cores with their corresponding Mopra IDs and CS (2–1) linewidths from Benedettini et al. (2012).

| SCUBA-2 ID | Mopra ID | $\Delta v$ (km s$^{-1}$) |
|---|---|---|
| L1S2 1 | Lup1_C4 | 0.72 ± 0.07 |
| L1S2 2 | Lup1_C6 | 0.54 ± 0.07 |
| L1S2 5 | Lup1_C7 | 0.87 ± 0.06 |
| L1S2 6 | Lup1_C8 | 0.62 ± 0.07 |
| L1S2 7 | Lup1_C3 | 0.99 ± 0.08 |

five separate cores, then there will be a greater number of cores in Lupus I, with a lower mean mass.

#### *5.1.4 Comparison to cores identified by Mopra*

Benedettini et al. (2012) used molecular line data obtained with the Mopra telescope to map the Lupus I, III and IV molecular clouds. In Lupus I, the observations cover the main ridge (B228). They identify eight cores in this region, with five corresponding to ones identified by SCUBA-2 (Lup1_C3, 4, 6, 7 and 8 corresponding to L1S2 7, 1, 2, 5 and 6, respectively). Emission lines from several molecular tracers were observed by Mopra, including $NH_3$, $N_2H^+$, $HC_3N$, CS and $CH_3OH$. Cores were then identified using whichever tracer best-defined the clump. The five matching cores are listed with CS (2–1) transition line-width information in Table 14.

SCUBA-2 identifies cores not seen with Mopra, and the reverse is also true (although the three most massive cores identified by SCUBA-2 are also seen with Mopra). SCUBA-2 has identified up to seven cores that Mopra did not detect, including two in the SW field not observed with Mopra. Some will likely be due to the clustered sources in the E field being detected as single objects by the larger Mopra beam, which, at 3 mm, is 35 arcsec. This low resolution means that particularly in the vicinity of L1S2 5, Mopra may also have picked up emission from the nearby cores identified by SCUBA-2 (3 and 4). Additionally, L1S2 6 lies near L1S2 8 and L1S2 10, meaning that these could also be effectively merged into the single Mopra core Lup1_C8.

Three cores were identified with Mopra that SCUBA-2 did not detect. All three of these cores (C1, C2 and C5) were detected weakly, or not at all, in $NH_3$ and $N_2H^+$. These species effectively trace the denser, inner regions of cores (Di Francesco et al. 2007) and an abundance of these molecules is indicative of a more evolved core (pre-stellar or protostellar). This therefore suggests that these three cores are starless and represent relatively low-density extended emission. The SCUBA-2 data reduction process suppresses large-scale areas of emission without strong central peaks of emission (Mairs et al. 2015). This suppression happens to a greater extent than with, for example, the *Herschel* 500 μm observations of Lupus I (Rygl et al. 2013). Therefore, extended cores without strong emission peaks, such as these three, can fail to appear in the SCUBA-2 map while still being identified by other instruments (Ward-Thompson et al. 2016).

### 5.2 Stability analysis

The Jeans mass for each of the cores was estimated using the relation from Chabrier (2003),

$$\frac{M_{\rm J}}{\rm M_\odot} = 1.2 \left(\frac{T}{10\,\rm K}\right)^{3/2} \left(\frac{\langle n_0\rangle}{10^4\,\rm cm^{-3}}\right)^{-1/2}, \quad (10)$$

where $T$ is the temperature of the core and $\langle n_0\rangle$ is the average number density of molecules (assumed to be hydrogen and helium). Jeans masses for all cores are provided in Table 13.

The average number density of molecules is given by $\langle n_0\rangle = M/\mu \rm m_p V$, where $M$ is the mass of the core calculated using the submillimetre continuum flux, $\mu$ is the assumed mean molecular mass (for the combination of $H_2$ and He) of 2.38 (Kauffmann et al. 2008). and $m_{\rm p}$ is the mass of a proton. $V$ is the ellipsoidal volume of the source, calculated from the core radius given in Table 13. The same temperatures were used to calculate the Jeans mass for each core as were used in calculating the core masses (see Table 12).

Less massive cores, for which the calculated submillimetre continuum mass is below the estimated Jeans mass, are sufficiently supported against gravitational collapse by thermal motions alone. For some, this state implies they will not collapse to form YSOs in the first place. Other sub-Jeans cores correspond to areas that have already formed YSOs, such as L1S2 4. This core contains the object L1YSO 11 (HT Lup), and thus has already undergone collapse in the past and will not fragment further. Additional sub-Jeans cores in which class II YSOs can be found are L1S2 6 and L1S2 9 (with L1YSOs 14 and 10, respectively).

Under the assumption that only thermal pressure is available to support against gravitational collapse, the Jeans mass suggests that the three larger, more massive cores in this sample (L1S2 1, L1S2 2 and L1S2 7) should be unstable against gravitational collapse, due to having masses significantly larger than the estimated Jeans mass for a core with similar density and temperature. However, L1S2 1 already contains the protostar L1YSO 7. As such, it would no longer be expected to satisfy the Jeans stability criterion.

Stability was also examined by calculating the virial mass for cores, when molecular line-width data from Benedettini et al. (2012) was available. Virial masses were calculated using the relation

$$M_{\rm vir} = \frac{5}{3}\frac{(\Delta v)^2 R}{\rm G}, \quad (11)$$

where $R$ is the radius of a core when treated as spherical and $G$ is the gravitational constant. $\Delta v$ is the 3D velocity dispersion of an observed tracer molecule in the cloud (in this case, CS (2–1), with 1D velocity dispersions given in Table 14).

The virial parameter $\alpha_{\rm vir}$ (Bertoldi & McKee 1992) was calculated for each core with an available linewidth, with $\alpha = \rm M_{vir}/M_{850}$. In the simplest case of treating a core as a constant density sphere, $\alpha_{\rm vir} < 1$ would indicate that the core is supercritical. When the core is instead treated as a Bonnor–Ebert sphere (Ebert 1955; Bonnor 1956) or is elongated (Bertoldi & McKee 1992), supercriticality is found with cores where $\alpha_{\rm vir} < 2$ (Kauffmann, Pillai & Goldsmith 2013).

A total of five cores identified by Benedettini et al. (2012) with available CS (2–1) transition data (Lup1_C3, Lup1_C4, Lup1_C6, Lup1_C7 and Lup1_C8) were also observed by SCUBA-2. Observations of the CS (2–1) transition were used to calculate the virial mass as CS provides a better match to dust core size than the other available species (Di Francesco et al. 2007). The 1D linewidths $(\Delta v_{\rm 1D})^2$ were converted to 3D velocity dispersions $(\sigma_{\rm 3D})^2$ using the relation

$$(\sigma_{\rm 3D})^2 = \frac{3(\Delta v_{\rm 1D})^2}{8\ln 2}. \quad (12)$$

These linewidths, listed in Table 14, were used in calculating the critical virial mass for five of the identified dense cores in Lupus I (see Table 13).

Once non-thermal turbulent support is taken into account, these calculations show that four of the five cores (L1S2 1, 5, 6 and

7) are virially stable. The core L1S2 1 contains the known protostar IRAS 15398-3359 (Heyer & Graham 1989), identified as SSTc2d J154301.3-340915 by *Spitzer* (Chapman et al. 2007; Merín et al. 2008) and as L1YSO 7 in this paper. The presence of a protostar in this core indicates that it has already undergone gravitational collapse. Indeed, indications of infall towards this source in *Herschel* water spectra were observed by Mottram et al. (2013). The calculation of virial masses using equation (11) assumes that the CS (2–1) linewidth is produced by turbulent motions that are able to support against collapse. This would not be the case if the linewidths were a result of outflowing/infalling material from a central object, as may be the case with L1S2 1/L1YSO 7.

L1S2 7 has a mass greater than its associated Jeans mass, but the virial parameter for this core is 5.5. This difference may be an indication that turbulent support in L1S2 7 is more important than thermal support. The proximity of L1S2 7 to L1S2 1, which contains L1YSO 7, could mean that turbulent activity has been induced by this nearby star formation. However, the CS (2–1) linewidths are all supersonic. This suggests that the cores are being supported by an additional support mechanism, perhaps pressure confinement (Pattle et al. 2015), which is preventing the turbulent pressure from breaking them apart.

The final core of the five, L1S2 2, has a virial parameter of $1.1 \pm 0.4$. This indicates that the core may be virially unstable and about to undergo gravitational collapse. The potential instability of L1S2 2 is notable given that there are no known YSOs within this core (with the nearest being L1YSO 9 at the edge), though the close proximity of L1YSOs 9, 10 and 11 shows a history of star formation in the vicinity of L1S2 2. With a mass of 2.99 $M_\odot$, it could be in the very earliest stages of birthing new stars. If there are deeply embedded YSOs in this core, then they would be expected to produce outflows of material.

The virial analysis here has shown L1S2 7 to be virially stable, and L1S2 2 to be potentially unstable. This difference indicates that starless, super-Jeans cores may be reaching the pre-stellar stage, or they may actually be subcritical thanks to additional support over thermal motions. Sadavoy, Di Francesco & Johnstone (2010) examine 17 cores with masses greater than their Jeans mass, previously classified as starless. They find three are genuinely starless, similar to L1S2 2 and L1S2 7. These cores may be supported by non-thermal motions, or they may also be virially unstable precursors to star formation. Pattle et al. (2015) find one of these starless cores, in Ophiuchus, to have a lower mass than calculated in Sadavoy et al. (2010). These newer observations with SCUBA-2 indicate that this core may not be super-Jeans at all.

Mairs et al. (2016) find two seemingly gravitationally unstable objects in Southern Orion A that contain no known YSOs. The contrast in virial stability between L1S2 2 and L1S2 7 indicates that such objects may or may not be pre-stellar. This is also seen by Pattle et al. (2015); of the four cores in Ophiuchus (out of 23) that are clearly gravitationally bound, three are virially bound (so pre-stellar) and one is not (though uncertainties mean that this is not definitive). Overall, it seems that the incidence of a low number of both starless and pre-stellar super-Jeans cores is typical in Gould Belt clouds. Southern Orion A is, however, a much more massive cloud than Lupus I, with an extinction-derived mass within the SCUBA-2 footprint of $9.5 \times 10^4$ $M_\odot$, compared to the distance-adjusted value for Lupus I of $\sim$250 $M_\odot$. Additionally, the total mass of the islands observed by SCUBA-2 is $1.3 \times 10^3$ $M_\odot$ in Southern Orion A, and only 8.7 $M_\odot$ in Lupus I. This seems to suggest that Lupus I shows a larger incidence of super-Jeans cores, but caution should be exercised with this assessment, as the total number of cores in Lupus I (12) is small.

## 6 SUMMARY AND CONCLUSIONS

In this study, both point-like sources (assumed to be YSOs) and extended emission (assumed to be protostellar, pre-stellar or starless cores) were extracted from the JCMT GBS SCUBA-2 maps of the Lupus I molecular cloud. YSOs were extracted using aperture photometry while extended objects were identified using the FellWalker source extraction algorithm. These observations have provided evidence for both ongoing and potential future star formation within Lupus I.

11 previously identified YSOs were detected by SCUBA-2 at 850 μm. Of these, four were also detected at 450 μm. One of the 11 sources is Class 0, one is Class I, one is a Class F and the rest are Class II; no Class III sources were detected by SCUBA-2. This distribution of Classes and evidence of ongoing star formation is similar to that found in the Ophiuchus north region, also in Sco-Cen (Hatchell et al. 2012), and contrasts with the low number of Class I and high number of Class III sources in Lupus III (Merín et al. 2008).

The overall fraction of YSOs in Lupus I that are protostellar (Including Class F) is consistent with that seen in other Gould Belt regions, such as Ophiuchus and Serpens (Dunham et al. 2015). However, the fraction of Class 0/I YSOs is greater in Lupus I (16 per cent versus 11 per cent), while the Class III fraction is low (16 per cent versus 40 per cent), suggesting that it is younger than many other Gould Belt clouds. Four additional YSOs detected by *Spitzer* were too faint to be detected by SCUBA-2, leading to a total of 15 YSOs being analysed further here.

For the 10 more evolved Class II and III sources, as well as two Class F sources, calculations of disc mass from submillimetre continuum emission (assuming $T = 20$ K and $\beta = 1$) reveal only one source has a disc mass of over the MMSN. This single occurrence is consistent with 2/20 YSOs detected by SCUBA-2 in Taurus L1495 having disc masses greater than the MMSN (Buckle et al. 2015). Among the nine Class F and II sources, the mean circumstellar disc mass is $5.9 \times 10^{-3}$ $M_\odot$.

For the three less-evolved Class 0 and I YSOs, as well as the two Class F YSOs, protostellar envelope masses and temperatures, were estimated using opacity-modified blackbody SED envelope fits for the three sources that were detected by SCUBA-2. When a less-evolved source was not detected by SCUBA-2, an upper limit to envelope mass was instead calculated. All of these envelope masses are low enough that any YSOs produced would be low-mass stars, brown dwarfs or even sub-brown dwarfs. Temperatures were found to be greater than the typical value of 14 K, particularly for L1YSO 1 (T = 28.8 K) that is located off the main ridge in the SW field.

Bolometric temperatures and luminosities were calculated for all 15 YSOs. Classifications based on $T_{\rm bol}$ largely match those based on spectral index. Three have $L_{\rm bol} < 0.1$ $L_\odot$ and another three have $L_{\rm bol} > 1$ $L_\odot$, with the rest lying within this range. The embedded YSOs with $L_{\rm bol} \leq 0.1$ $L_\odot$, L1YSO 2 and L1YSO 9 are therefore VeLLOs. A third source with $L_\star \sim 0.1$ $L_\odot$, L1YSO 5, is also consistent with being a VeLLO, due to a large uncertainty on $L_{\rm bol}$. Furthermore, a fourth source, L1YSO 1, may be an example of a protostellar VeLLO being heated to a higher bolometric luminosity by the interstellar radiation field. This number of VeLLOs represents a larger fraction of VeLLOs than was found by Dunham et al. (2008) across the *Spitzer* c2d survey regions.

SEDs for all 15 YSOs within the field of view of SCUBA-2 in Lupus I were produced. The model SEDs of Robitaille et al. (2006) were fit to the observed fluxes for each YSO. Statistical tests were used to separate well-fitting SEDs from poorly fit ones. Where multiple models provided good fits to the SED of a particular YSO, the ranges of disc masses, envelope masses and interstellar extinction values were found. In general, the parameter most effectively constrained by these models was the interstellar extinction, with large degeneracies being found in disc and envelope masses. The upcoming *Herschel* point source catalogue for Lupus I will provide further data in the submillimetre regime, which should facilitate improved models.

An updated SFR for Lupus I, of 2.6 $\pm$ 0.6 $M_\odot$ $Myr^{-1}$, was calculated. Whilst this is low compared to many other Gould Belt regions, the low mass of Lupus I means that it is not unusual.

Next, 12 areas of extended emission, corresponding to starless, pre-stellar or protostellar cores were found in the SCUBA-2 850 μm map. Across all 12, the mean mass is 0.73 $M_\odot$ and the total mass is 8.7 $M_\odot$, approximately 1/20 of the total mass in the main part of the cloud.

Values for the thermal Jeans mass are estimated for each of these cores, with values between 0.3 and 1.1 $M_\odot$. The three largest cores are not Jeans stable. One of these cores, however, contains a known protostar; therefore, two starless super-Jeans cores are detected in Lupus I. This is consistent with observations in southern Orion A by Mairs et al. (2016), which also contain two starless super-Jeans cores.

Virial stability analysis, including non-thermal linewidths, is thus also performed using CS (2–1) transition data for five sources in Lupus I. Four sources are found to be stable against collapse, including one of the starless super-Jeans cores. The fifth core is virially bound, with a virial parameter of 1.1 $\pm$ 0.4. This core, L1S2 2, contains no known YSO detections and has a mass of 2.99 $M_\odot$. This core may therefore be a pre-stellar core candidate, meriting further observations.

The presence of a pre-stellar core candidate, and the high Class 0/I to Class III YSO ratio of 1:1, provides further evidence that a star formation event in Lupus I has been triggered recently by a shock (Gaczkowski et al. 2015).

## ACKNOWLEDGEMENTS

The JCMT has historically been operated by the Joint Astronomy Centre on behalf of the Science and Technology Facilities Council (STFC) of the United Kingdom, the National Research Council of Canada and the Netherlands Organisation for Scientific Research. Additional funds for the construction of SCUBA-2 were provided by the Canada Foundation for Innovation. The identification number for the programme under which the SCUBA-2 data used in this paper was obtained is MJLSG34. Chris Mowat is supported by an STFC studentship.

This research has made use of NASA's Astrophysics Data System. This research used the services of the Canadian Advanced Network for Astronomy Research (CANFAR) which in turn is supported by CANARIE, Compute Canada, University of Victoria, the National Research Council of Canada and the Canadian Space Agency. This research used the facilities of the Canadian Astronomy Data Centre operated by the National Research Council of Canada with the support of the Canadian Space Agency.

Starlink software (Currie et al. 2014) is supported by the East Asian Observatory. MATPLOTLIB is a 2D graphics package used for PYTHON for application development, interactive scripting and publication-quality image generation across user interfaces and operating systems. This research made use of APLPY (Robitaille & Bressert 2012), an open-source plotting package for PYTHON hosted at http://aplpy.github.com.

This publication makes use of data products from the Wide-field Infrared Survey Explorer, which is a joint project of the University of California, Los Angeles, and the Jet Propulsion Laboratory/California Institute of Technology, funded by the National Aeronautics and Space Administration. This publication makes use of data products from the 2MASS that is a joint project of the University of Massachusetts and the Infrared Processing and Analysis Center/California Institute of Technology, funded by the National Aeronautics and Space Administration and the National Science Foundation. This research uses observations with AKARI, a JAXA project with the participation of ESA. *Herschel* is an ESA space observatory with science instruments provided by European-led Principal Investigator consortia and with important participation from NASA.

The authors wish to recognize and acknowledge the very significant cultural role and reverence that the summit of Maunakea has always had within the indigenous Hawaiian community. We are most fortunate to have the opportunity to conduct observations from this mountain. The authors would also like to thank the anonymous referee for their help in clarifying the content of this paper.

## REFERENCES

Adams F. C., Lada C. J., Shu F. H., 1987, ApJ, 312, 788
André P., Ward-Thompson D., Barsony M., 1993, ApJ, 406, 122
André P. et al., 2010, A&A, 518, L102
Andrews S. M., Williams J. P., 2005, ApJ, 631, 1134
Andrews S. M., Williams J. P., 2007, ApJ, 659, 23
Aniano G., Draine B. T., Gordon K. D., Sandstrom K., 2011, PASP, 123, 1218
Antoniucci S., Giannini T., Li Causi G., Lorenzetti D., 2014, ApJ, 782, 51
Azimlu M., Martínez-Galarza J. R., Muench A. A., 2015, AJ, 150, 95
Baade D. et al., 1999, The Messenger, 95, 15
Barnard E. E., 1927, Catalogue of 349 Dark Objects in the Sky. Univ. Chicago Press, Chicago
Beckwith S. V. W., Sargent A. I., 1991, ApJ, 381, 250
Beckwith S. V. W., Sargent A. I., Chini R. S., Guesten R., 1990, AJ, 99, 924
Beichman C. A., Neugebauer G., Habing H. J., Clegg P. E., Chester T., 1988, Infrared Astronomical Satellite (IRAS) Catalogs and Atlases. Volume 1: Explanatory Supplement
Benedettini M., Pezzuto S., Burton M. G., Viti S., Molinari S., Caselli P., Testi L., 2012, MNRAS, 419, 238
Berry D. S., 2015, Astron. Comput., 10, 22
Berry D. S., Reinhold K., Jenness T., Economou F., 2013, Astrophysics Source Code Library, record ascl:1311.007
Bertoldi F., McKee C. F., 1992, ApJ, 395, 140
Bessell M. S., 1979, PASP, 91, 589
Bonnor W. B., 1956, MNRAS, 116, 351
Booth R. S. et al., 1989, A&A, 216, 315
Buckle J. V. et al., 2015, MNRAS, 449, 2472
Bustamante I., Merín B., Ribas Á., Bouy H., Prusti T., Pilbratt G. L., André P., 2015, A&A, 578, A23
Cambrésy L., 1999, A&A, 345, 965
Chabrier G., 2003, PASP, 115, 763
Chapin E. L., Berry D. S., Gibb A. G., Jenness T., Scott D., Tilanus R. P. J., Economou F., Holland W. S., 2013, MNRAS, 430, 2545
Chapman N. L. et al., 2007, ApJ, 667, 288
Chen M. et al., 2016, ApJ, 826, 95
Cohen M., Wheaton W. A., Megeath S. T., 2003, ApJ, 126, 1090

Comerón F., 2008, in Reipurth B., ASP Monograph Publications, Vol. 5, Handbook of Star Forming Regions, Vol. II, The Lupus Clouds. Astron. Soc. Pac., San Francisco, p. 295
Comerón F., Spezzi L., López Martí B., 2009, A&A, 500, 1045
Currie M. J., Berry D. S., 2013, Starlink User Note, 95
Currie M. J., Berry D. S., Jenness T., Gibb A. G., Bell G. S., Draper P. W., 2014, in Manset N., Forshay P., eds., ASP Conf. Ser. Vol. 485, Astronomical Data Analysis Software and Systems XXIII. Astron. Soc. Pac., San Francisco, p. 391
Cutri R. M. et al., 2003, VizieR Online Data Catalog, 2246
Cutri R. M. et al., 2012, VizieR Online Data Catalog, 2311
de Geus E. J., 1992, A&A, 262, 258
Dempsey J. T. et al., 2013, MNRAS, 430, 2534
Di Francesco J., Evans N. J., II, Caselli P., Myers P. C., Shirley Y., Aikawa Y., Tafalla M., 2007, in Reipurth B., Jewitt D., Keil K., eds, Protostars and Planets V. Univ. Arizona Press, Tucson, AZ, p. 17
Dodds P., Greaves J. S., Scholz A., Hatchell J., Holland W. S., JCMT Gould Belt Survey Team, 2015, MNRAS, 447, 722
Draper P. W., Berry D. S., Jenness T., Economou F., 2009, in Bohlender D. A., Durand D., Dowler P., eds., ASP Conf. Ser. Vol. 411, Astronomical Data Analysis Software and Systems XVIII. Astron. Soc. Pac., San Francisco, p. 575
Dunham M. M., Vorobyov E. I., 2012, ApJ, 747, 52
Dunham M. M., Crapsi A., Evans N. J., II, Bourke T. L., Huard T. L., Myers P. C., Kauffmann J., 2008, ApJS, 179, 249
Dunham M. M. et al., 2013, AJ, 145, 94
Dunham M. M. et al., 2015, ApJS, 220, 11
Ebert R., 1955, Z. Astrophys., 37, 217
Enoch M. L., Evans N. J., II, Sargent A. I., Glenn J., 2009, ApJ, 692, 973
Evans N. J., II et al., 2003, PASP, 115, 965
Evans N. et al., 2009, ApJS, 181, 321
Faimali A. et al., 2012, MNRAS, 426, 402
Fazio G. G. et al., 2004, ApJS, 154, 10
Forbrich J., Tappe A., Robitaille T., Muench A. A., Teixeira P. S., Lada E. A., Stolte A., Lada C. J., 2010, ApJ, 716, 1453
Gaczkowski B. et al., 2015, A&A, 584, A36
Galli P. A. B., Bertout C., Teixeira R., Ducourant C., 2013, A&A, 558, A77
Galli P. A. B., Bertout C., Teixeira R., Ducourant C., 2015, A&A, 580, A26
Gibb A. G., Jenness T., Economou F., 2013, Starlink User Note, 265
Greene T. P., Wilking B. A., Andre P., Young E. T., Lada C. J., 1994, ApJ, 434, 614
Griffin M. J. et al., 2010, A&A, 518, L3
Hatchell J. et al., 2012, ApJ, 754, 104
Hatchell J. et al., 2013, MNRAS, 429, L10
Heiderman A., Evans N. J., II, Allen L. E., Huard T., Heyer M., 2010, ApJ, 723, 1019
Heyer M. H., Graham J. A., 1989, PASP, 101, 816
Hildebrand R. H., 1983, Q. J. R. Astron. Soc., 24, 267
Holland W. S. et al., 2013, MNRAS, 430, 2513
Hughes J., Hartigan P., Krautter J., Kelemen J., 1994, AJ, 108, 1071
Ishihara D. et al., 2010, A&A, 514, A1
Jarrett T. H. et al., 2011, ApJ, 735, 112
Kackley R., Scott D., Chapin E., Friberg P., 2010, in Radziwill N., Bridger A., eds, Proc. SPIE Conf. Ser. Vol. 7740, Software and Cyberinfrastructure for Astronomy. SPIE, Bellingham, p. 77401Z
Kauffmann J., Bertoldi F., Bourke T. L., Evans N. J., II, Lee C. W., 2008, A&A, 487, 993
Kauffmann J., Pillai T., Goldsmith P. F., 2013, ApJ, 779, 185
Kawada M. et al., 2007, PASJ, 59, 389
Kim S.-H., Martin P. G., Hendry P. D., 1994, ApJ, 422, 164
Kirk H., Johnstone D., Di Francesco J., 2006, ApJ, 646, 1009
Kirk H. et al., 2016, ApJ, 817, 167
Kristensen L. E. et al., 2012, A&A, 542, A8
Kukarkin B. V., Kholopov P. N., Pskovsky Y. P., Efremov Y. N., Kukarkina N. P., Kurochkin N. E., Medvedeva G. I., 1971, General Catalogue of Variable Stars, 3rd edn. Sternberg Astronomical Institute, Moscow
Lombardi M., Lada C. J., Alves J., 2008, A&A, 480, 785
McKee C. F., Ostriker E. C., 2007, ARA&A, 45, 565
Mairs S. et al., 2015, MNRAS, 454, 2557
Mairs S. et al., 2016, MNRAS, 461, 4022
Merín B. et al., 2008, ApJS, 177, 551
Mottram J. C. et al., 2011, A&A, 525, A149
Mottram J. C., van Dishoeck E. F., Schmalzl M., Kristensen L. E., Visser R., Hogerheijde M. R., Bruderer S., 2013, A&A, 558, A126
Murakami H. et al., 2007, PASJ, 59, 369
Myers P. C., Ladd E. F., 1993, ApJ, 413, L47
Neugebauer G. et al., 1984, ApJ, 278, L1
Nuernberger D., Chini R., Zinnecker H., 1997, A&A, 324, 1036
Onaka T. et al., 2007, PASJ, 59, 401
Ossenkopf V., Henning T., 1994, A&A, 291, 943
Oya Y. et al., 2014, ApJ, 795, 152
Pattle K. et al., 2015, MNRAS, 450, 1094
Pecaut M., Mamajek E., Bubar E., 2012, ApJ, 746, 22
Pogson N., 1856, MNRAS, 17, 12
Prato L., Greene T. P., Simon M., 2003, ApJ, 584, 853
Preibisch T., Brown A. G. A., Bridges T., Guenther E., Zinnecker H., 2002, ApJ, 124, 13
Reach W. T. et al., 2005, PASP, 117, 978
Reid M. A., Wilson C. D., 2005, ApJ, 625, 891
Reipurth B., Chini R., Krugel E., Kreysa E., Sievers A., 1993, A&A, 273, 221
Rieke G. H. et al., 2004, ApJS, 154, 25
Rieke G. H. et al., 2008, AJ, 135, 2245
Robitaille T., Bressert E., 2012, Astrophysics Source Code Library, record ascl:1208.017
Robitaille T. P., Whitney B. A., Indebetouw R., Wood K., Denzmore P., 2006, ApJS, 167, 256
Robitaille T. P., Whitney B. A., Indebetouw R., Wood K., 2007, ApJS, 169, 328
Rumble D. et al., 2015, MNRAS, 448, 1551
Rumble D. et al., 2016, MNRAS, 460, 4150
Rygl K. L. J. et al., 2013, A&A, 549, L1
Sadavoy S. I., Di Francesco J., Johnstone D., 2010, ApJ, 718, L32
Salji C. J. et al., 2015, MNRAS, 449, 1769
Simpson J. P., Cotera A. S., Burton M. G., Cunningham M. R., Lo N., Bains I., 2012, MNRAS, 419, 211
Siringo G. et al., 2009, A&A, 497, 945
Skrutskie M. F. et al., 2006, AJ, 131, 1163
Spezzi L. et al., 2008, ApJ, 680, 1295
Tachihara K., Dobashi K., Mizuno A., Ogawa H., Fukui Y., 1996, PASJ, 48, 489
Tachihara K., Toyoda S., Onishi T., Mizuno A., Fukui Y., Neuhäuser R., 2001, PASJ, 53, 1081
Ward-Thompson D. et al., 2007, PASP, 119, 855
Ward-Thompson D. et al., 2016, MNRAS, 463, 1008
Weingartner J. C., Draine B. T., 2001, ApJ, 548, 296
Werner M. W. et al., 2004, ApJS, 154, 1
Whitney B. A., Wood K., Bjorkman J. E., Cohen M., 2003, ApJ, 598, 1079
Wilking B. A., Lada C. J., Young E. T., 1989, ApJ, 340, 823
Williams J. P., de Geus E. J., Blitz L., 1994, ApJ, 428, 693
Wright E. L. et al., 2010, AJ, 140, 1868
Yamamura I., Makiuti S., Ikeda N., Fukuda Y., Oyabu S., Koga T., White G. J., 2010, VizieR Online Data Catalog, 2298
Zacharias N., Monet D. G., Levine S. E., Urban S. E., Gaume R., Wycoff G. L., 2005, VizieR Online Data Catalog, 1297

## SUPPORTING INFORMATION

Supplementary data are available at *MNRAS* online.

**supplementary_info.pdf**

Please note: Oxford University Press is not responsible for the content or functionality of any supporting materials supplied by

the authors. Any queries (other than missing material) should be directed to the corresponding author for the article.

[1]*Physics and Astronomy, University of Exeter, Stocker Road, Exeter EX4 4QL, UK*
[2]*NRC Herzberg Astronomy and Astrophysics, 5071 West Saanich Rd, Victoria, BC, V9E 2E7, Canada*
[3]*Astrophysics Group, Cavendish Laboratory, J J Thomson Avenue, Cambridge CB3 0HE, UK*
[4]*Kavli Institute for Cosmology, Institute of Astronomy, University of Cambridge, Madingley Road, Cambridge CB3 0HA, UK*
[5]*Joint Astronomy Centre, 660 N. A'ohōkū Place, University Park, Hilo, Hawaii 96720, USA*
[6]*Department of Physics and Astronomy, University of Victoria, Victoria, BC, V8P 1A1, Canada*
[7]*LSST Project Office, 933 N. Cherry Ave, Tucson, AZ 85719, USA*
[8]*Leiden Observatory, Leiden University, PO Box 9513, NL-2300 RA Leiden, the Netherlands*
[9]*Max-Planck Institute for Astronomy, Königstuhl 17, D-69117 Heidelberg, Germany*
[10]*Jeremiah Horrocks Institute, University of Central Lancashire, Preston, Lancashire PR1 2HE, UK*
[11]*Department of Physics and Astronomy, University of Waterloo, Waterloo, Ontario, N2L 3G1, Canada*
[12]*Université de Montréal, Centre de Recherche en Astrophysique du Québec et département de physique, C.P. 6128, succ. centre-ville, Montréal, QC, H3C 3J7, Canada*
[13]*James Madison University, Harrisonburg, Virginia 22807, USA*
[14]*School of Physics, Astronomy and Mathematics, University of Hertfordshire, College Lane, Hatfield, HERTS AL10 9AB, UK*
[15]*National Science Foundation, Division of Astronomical Sciences, Arlington, VA 22230, USA*
[16]*Imperial College London, Blackett Laboratory, Prince Consort Rd, London SW7 2BB, UK*
[17]*School of Physics and Astronomy, Cardiff University, The Parade, Cardiff CF24 3AA, UK*
[18]*Deparment of Physics and Astronomy, University of Manitoba, Winnipeg, Manitoba, R3T 2N2, Canada*
[19]*Dunlap Institute for Astronomy and Astrophysics, University of Toronto, 50 St. George St, Toronto, ON, M5S 3H4, Canada*
[20]*Jodrell Bank Centre for Astrophysics, Alan Turing Building, School of Physics and Astronomy, University of Manchester, Oxford Road, Manchester M13 9PL, UK*
[21]*UK Astronomy Technology Centre, Royal Observatory, Blackford Hill, Edinburgh EH9 3HJ, UK*
[22]*Institute for Astronomy, Royal Observatory, University of Edinburgh, Blackford Hill, Edinburgh EH9 3HJ, UK*
[23]*Centre de recherche en astrophysique du Québec et Département de physique, de génie physique et d'optique, Université Laval, 1045 avenue de la médecine, Québec, G1V 0A6, Canada*
[24]*Department of Physics and Astronomy, UCL, Gower St, London WC1E 6BT, UK*
[25]*Department of Physics and Astronomy, McMaster University, Hamilton, ON, L8S 4M1, Canada*
[26]*Department of Physics, University of Alberta, Edmonton, AB T6G 2E1, Canada*
[27]*Harvard-Smithsonian Center for Astrophysics, 60 Garden Street, Cambridge, MA 02138, USA*
[28]*University of Western Sydney, Locked Bag 1797, Penrith NSW 2751, Australia*
[29]*Department of Physical Sciences, The Open University, Milton Keynes MK7 6AA, UK*
[30]*The Rutherford Appleton Laboratory, Chilton, Didcot OX11 0NL, UK*
[31]*National Astronomical Observatory of China, 20A Datun Road, Chaoyang District, Beijing 100012, China*

This paper has been typeset from a TEX/LATEX file prepared by the author.